GDN1 against N-terminal region of *Drosophila* presenilin (Psn) was previously described (21). Rabbit polyclonal antibody SPP_{CT} against the C terminus (358–377) of human SPP was kindly provided by Dr. Todd Golde (University of Florida) (22). Mouse monoclonal antibodies were purchased from Sigma (anti-FLAG M2), Invitrogen (anti-V5), Qiagen (Hilden, Germany) (anti-His$_4$), and Cell Signaling Technology (Danvers, MA) (anti-c-Myc 9B11), respectively. [(2*R*,4*R*,5*S*)-2-Benzyl-5-(*t*-butyloxycarbonylamino)-4-hydroxy-6-phenylhexanoyl]-L-leucyl-L-phenylalanine amide (L-685,458) (23) and 1,3-di-(*N*-carboxybenzoyl-L-leucyl-L-leucyl)amino acetone ((Z-LL)$_2$-ketone) (12) were purchased from the PEPTIDE INSTITUTE INC. (Osaka, Japan). pep.11 and pep.11-Bt were synthesized by BEX Co., LTD (Tokyo, Japan). L-852,505, L-852,646, Dibenzazepine (DBZ), DBZ-BpB3, 31C, and 31C-Bpa were kindly provided by Drs. Yueming Li (Memorial Sloan-Kettering Cancer Center, NY), Haruhiko Fuwa (Tohoku University, Miyagi, Japan) Naoki Umezawa and Tsunehiko Higuchi (Nagoya City University, Aichi, Japan) (23–25).

Construction of Expression DNA Plasmids, Cell Culture, Recombinant Baculovirus Generation, and Transfection—Full-length cDNAs encoding wild-type (WT) human SPP as well as D219A mutant SPP (kindly provided by Dr. Evgeny I. Rogaev (University of Massachusetts Medical School) (17)) were inserted into pCMV10 (Sigma) vector to add 3×FLAG tag at the N terminus. 3×FLAG-tagged human SPP (3FSPP) cDNAs were then inserted into pFASTBac 1 vector (Invitrogen). cDNA encoding 3FSPP/NT in pFASTBac 1 vector was synthesized by PCR. cDNAs encoding full-length dSPP and dSPP/NT were amplified using I.M.A.G.E. clone SD07518 and inserted into pAc5.1/V5-His B vector (Invitrogen). Aspartate mutant dSPP (*i.e.* D228A or D274A) as well as dSPP/NT was generated by PCR. cDNAs encoding SPP_{sub} (kindly provided by Drs. Andrew Nyborg and Todd Golde) (22) as well as *Renilla* luciferase (Promega) were subcloned into pIB/V5-His/TOPO vector (Invitrogen). Endoplasmic reticulum stress response element (ERSE)-fused firefly luciferase construct (kindly provided by Dr. Kazutoshi Mori (Kyoto University, Kyoto, Japan) (26)) was inserted into pIZT/V5-His vector (Invitrogen). Expression construct for SPPL2b in pEF4/myc-His (Invitrogen) was provided by Drs. Regina Fluhler and Christian Haass (Ludwig-Max-imilians-University, München, Germany) (19). All constructs were sequenced using Thermo Sequenase (GE Healthcare) on an automated sequencer (LI-COR Biosciences, Lincoln, NE). Recombinant baculovirus was generated according to the manufacturer's instructions. Maintenance and transfection of S2 and Sf9 cells were performed as described previously (11, 21, 27, 28). Sf9 cells (2 × 10^6 cells/ml) were infected with a combination of recombinant baculoviruses at the virus volume of maximum expression level and harvested 72 h after infection.

Sample Preparation, Immunoprecipitation, Photoaffinity Labeling, Electrophoresis, and Immunoblotting—The cells were homogenized in 10% w/v glycerol-containing HEPES buffer (10 mM HEPES, pH 7.4, 150 mM NaCl, and Complete protease inhibitor mixture (Roche Applied Science)) and subsequently centrifuged at 1,000 × *g* for 10 min. The supernatants were centrifuged again at 100,000 × *g* for 60 min to isolate the microsome fraction. The microsomes or cells were resuspended in 2%

n-dodecyl-β-D-maltopyranoside (DDM)-containing HEPES buffer to designate them as the solubilized microsomes or cell lysates. For large scale preparation, solubilized microsome fractions from infected Sf9 cells were loaded on anti-FLAG M2-agarose and eluted with 500 μg/ml 3×FLAG peptide-containing 2% DDM-containing HEPES buffer after being washed three times. Eluate was further separated by a Superose 6 HR 10/30 column (GE Healthcare) on an ÄKTA Explorer chromatography system (GE Healthcare). For immunoprecipitation, DDM-solubilized fractions were coincubated with primary antibody and protein G-agarose (Invitrogen). Photoaffinity labeling experiments were performed as described previously, with some modifications (24, 25, 29). Briefly, microsomal fractions or 0.25% DDM-solubilized fractions were incubated with 50 nM photoprobes (*i.e.* L-852,505, L-852,646) and then irradiated for 90 min. Irradiated samples were adjusted to 1% SDS and rocked with immobilized streptavidin (GE Healthcare) overnight. Biotinylated proteins were eluted with SDS sample buffer by heating for 1 min and subjected to immunoblotting. SDS-PAGE and immunoblotting were performed as described previously (30). Blue-Native PAGE (BN-PAGE) was performed according to the manufacturer's protocol (Invitrogen). Briefly, membrane fractions were suspended in NativePAGE™ sample buffer containing 1% DDM. The mixture was centrifuged for 10 min at 15,000 × *g*, and Coomassie Brilliant Blue was added to the supernatant to give a final concentration of 0.25% w/v. NativeMark™ unstained protein standard (Invitrogen) was used as a molecular weight standard. After electrophoresis, the gel was transferred to PVDF membranes. The membranes were destained briefly in methanol before being incubated with specific antibodies.

SPP Activity Assay—To measure SPP activity *in vitro*, solubilized samples were incubated with Myc-Prl-PP-FLAG peptide (BEX Co., Ltd.) (31) at 37 °C. For SPP reporter assay *in vivo* (22), constructs encoding dSPP, ERSE-firefly luciferase, SPP_{sub}, and *Renilla* luciferase were transfected to S2 cells. Luciferase activities were measured by the PicaGene Dual luciferase system (TOYO B-Net. Co., LTD. Tokyo, Japan) according to the manufacturer's instructions.

Transmission Electron Microscopy—Fractions were adsorbed by thin carbon films rendered hydrophilic by glow discharge in low air pressure and supported by copper mesh grids. Samples were washed with five drops of double-distilled water, negatively stained with 2% uranyl acetate solution for 30 s twice, blotted, and air-dried. For immuno-EM, purified 3FSPP and anti-FLAG M2 monoclonal antibody were mixed for 30 min at 4 °C, and excess antibodies were removed by gel filtration chromatography (SMART system (GE Healthcare)). Samples were then negatively stained as described. Micrographs of negatively stained particles were recorded in a JEOL 100CX transmission electron microscope (JEOL, Tokyo, Japan) at ×53,100 magnification with 100-kV acceleration voltages. Images were recorded on SO-163 films (Eastman Kodak Co.), developed with a D19 developer (Kodak) and digitized with a Scitex Leafscan 45 scanner (Leaf systems, Westborough, MA) at a pixel size of 1.92 Å at the specimen level.

Automated Particle Selection and Image Analysis—Single particle image analysis (32) was performed using our SPINNS

program and the IMAGIC V program (33–37). The projections were picked up by a combination of two automatic pickup programs: the auto-accumulation method using simulated annealing (34) and the three-layered neural network method (35). Initially, 531 particles, in 160 × 160-pixel subframes, were selected from five EM images and used to train a pyramid-type neural network. Using the trained neural network, 4,692 particles were selected. The images were band pass-filtered with a low frequency cutoff of 384 Å and a high frequency cutoff of 4 Å, using IMAGIC V. The following image analysis was performed in three steps. First, the 4,692 images were rotationally and translationally aligned using the reference-free method (35). The aligned images were then classified into 150 clusters by the modified growing neural gas network method using a circular mask (37). Images in each cluster were averaged, and the averages with circular mask were used as new references. This cycle, from alignment to averaging, was repeated 25 times. The Euler angles of the class averages were automatically determined by the echo-correlated three-dimensional reconstruction method with simulated annealing (36) assuming C4 symmetry because of the tetrameric subunit stoichiometry of 3FSPP. These angles were used to calculate a preliminary three-dimensional density map by the simultaneous iterative reconstruction technique (38). The reprojections from the volume were employed as references for multi-reference alignment, and each image in the library was aligned and classified, providing improved cluster averages. From these averages, a new three-dimensional map was generated by the reconstruction method using simulated annealing without a three-dimensional reference. This cycle was repeated for three cycles. The density map was further refined by projection matching (39) followed by echo-correlated reconstruction. This cycle was repeated until convergence. Resolution was assessed without masking by dividing the data into two subsets and then calculated using the independent three-dimensional reconstructions of each, which were compared by Fourier shell correlation at the threshold of 0.5, using IMAGIC V.

RESULTS

Proteolytically Active SPP Polypeptides Form a Multimeric Complex—To characterize the SPP molecule in an enzymatically active state, we analyzed endogenous SPP by BN-PAGE in the DDM-solubilized condition, in which SPP activity was preserved (31). Endogenous human SPP, which existed as a 45-kDa monomer and a heat-sensitive dimer (90 kDa) on SDS-PAGE analysis (40) (Fig. 1A), was detected as a single band at 200 kDa (Fig. 1B), suggesting that active SPP forms a high molecular mass complex in the DDM-solubilized condition. Next we analyzed *Drosophila* SPP, which is composed of 389 amino acids (18). Endogenous dSPP polypeptide in S2 cells was detected as a single band of 40 kDa on SDS-PAGE without extensive boiling, indicating that dSPP did not form the SDS-resistant dimer (Fig. 1C). However, DDM-solubilized dSPP was migrated as a 180-kDa high molecular mass complex (Fig. 1D). Notably, endogenous dSPP was specifically co-immunoprecipitated with exogenously overexpressed dSPP, but not with other multispanning proteins, similarly to mammalian SPP (Fig. 1E, supplemental Fig. S1A) (22, 40), suggesting that the ability of SPP to form a
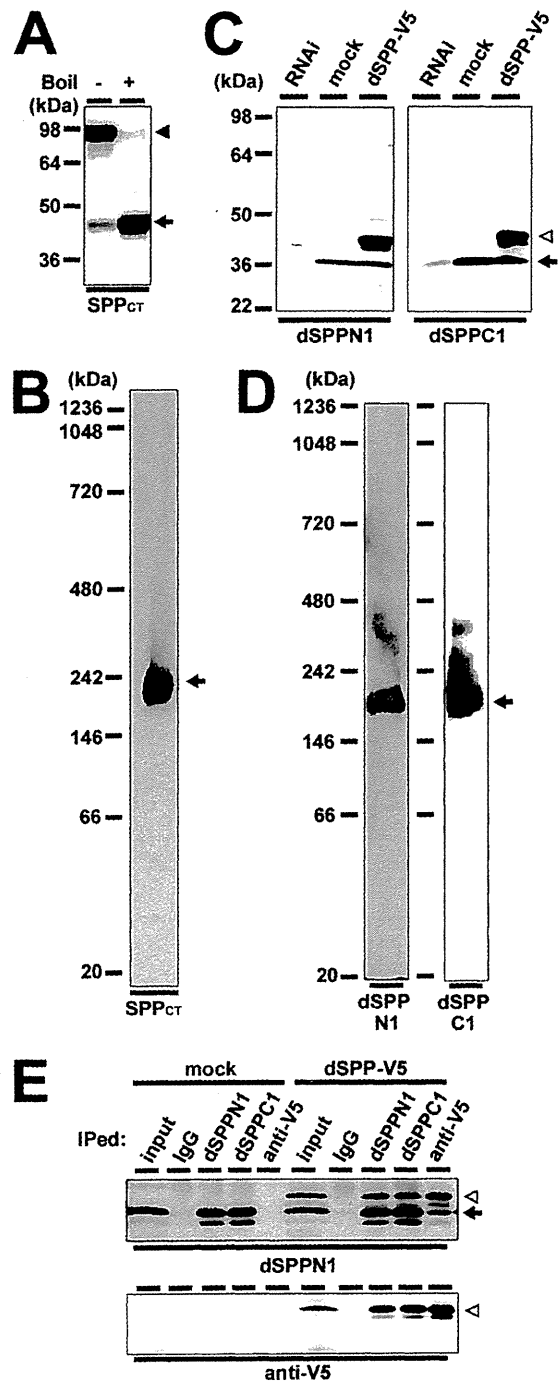

FIGURE 1. **Endogenous SPP proteins formed a high molecular weight complex in the enzymatically active state.** *A*, immunoblot analysis of SDS-solubilized HEK293 cell lysates. Samples were loaded with (+) or without (−) pre-boiling (*Boil*). The SDS-resistant dimer and monomer forms of SPP are indicated by the *black arrowhead* and *arrow*, respectively. *B*, SPP proteins (*black arrow*) in 0.25% DDM-solubilized HEK293 cell lysates were analyzed by BN-PAGE. *C*, immunoblot analysis of SDS-solubilized lysates of S2 cells transfected with dsRNA (*RNAi*), mock, or dSPP-V5. Endogenous and overexpressed dSPP proteins are indicated by the *black arrow* and *white arrowhead*, respectively. *D*, dSPP proteins (*black arrow*) in 0.25% DDM-solubilized S2 cell lysates were analyzed by BN-PAGE. *E*, immunoprecipitation of DDM-solubilized S2 cells transfected with mock or dSPP-V5 by antibodies indicated at the top of the panels. 10% of lysates was loaded as an input control. Endogenous and overexpressed dSPP proteins are indicated by the *black arrows* and *white arrowheads*, respectively. *IPed*, immunoprecipitated.
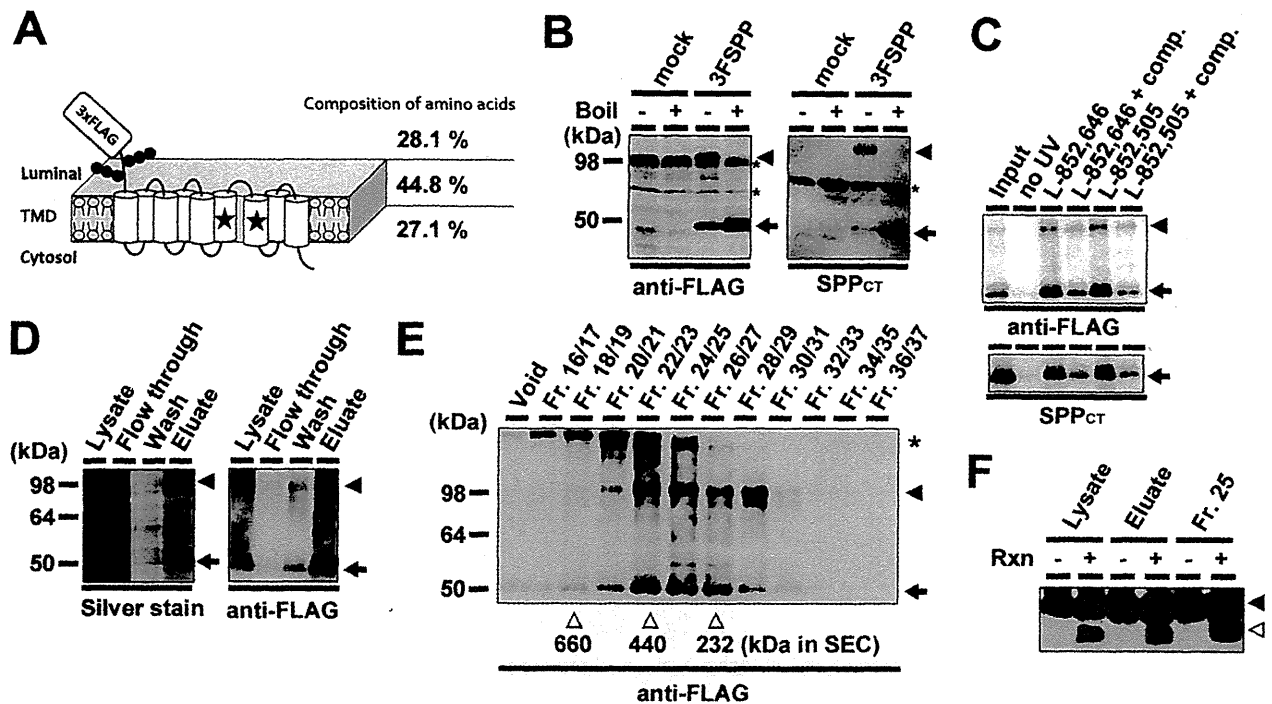
FIGURE 2. **Biochemical characterization of recombinant 3FSPP expressed in Sf9 cells.** *A*, schematic depiction of 3FSPP with predicted membrane topology. Catalytic aspartates are shown by *stars*. The *black circles* represent glycosylation. Ratios of each domain (*i.e.* luminal, transmembrane (*TMD*), and cytosolic domains), based on the composition of predicted amino acids, are indicated at the *right*. *B*, immunoblot analysis of lysates of Sf9 cells infected with recombinant baculovirus. Samples were loaded with (+) or without (−) pre-boiling (*Boil*). A heat-sensitive SDS-resistant dimer and monomer of 3FSPP are indicated by the *black arrowheads* and *black arrows*, respectively. The *asterisks* denote nonspecific bands. *C*, photoaffinity labeling experiment of infected Sf9 cell lysates with L-852,646, and L-852,505. Both probes successfully labeled 3FSPP, as indicated by the monomer (*black arrows*) as well as the dimer (*black arrowheads*), and the labeling was completely eliminated by the coincubation with the parent compound L-685,458 (*comp.*) *D*, affinity purification of 3FSPP from DDM-solubilized Sf9 cells using an anti-FLAG antibody column. The *arrows* and *arrowheads* indicate the monomer and dimer of 3FSPP, respectively. *E*, immunoblot analysis of affinity-purified 3FSPP separated by SEC using anti-FLAG M2 antibody. The *arrow* and *arrowhead* indicate the monomer and the dimer, respectively. Fractions (*Fr.*) containing SEC markers are represented by the *vertical white arrowheads* below the *upper panel*. *F*, proteolytic activity of purified 3FSPP *in vitro*. SPP substrate (*black arrowhead*) was cleaved to generate endoproteolytic product (*white arrowhead*) by coincubation at 37 °C (*Rxn* (+)) with infected Sf9 cell lysates, eluate of anti-FLAG antibody column (*B*), and fraction 25 of SEC (*C*).

homo-oligomer is conserved beyond species irrespective of the formation of SDS-resistant dimer. In addition, DDM-solubilized SPPL2b, of which the mature form migrated at 90 kDa on SDS-PAGE (19), was detected at 400 kDa on BN-PAGE (supplemental Fig. S1, *B* and *C*). These data suggest that SPP protease family proteins maintain the high molecular weight complex structure in the DDM-solubilized condition.

To examine whether high molecular weight SPP complex is composed solely of SPP polypeptides or incorporates other components, we overexpressed 3FSPP (Fig. 2*A*) by the recombinant baculovirus/Sf9 cell system. 3FSPP polypeptide, which migrated at 50 kDa as a monomeric form, was detected as a heat-sensitive, SDS-resistant 100-kDa dimer on SDS-PAGE similarly to that in mammalian cells (Fig. 2*B*). DDM-solubilized Sf9 cell lysates exhibited a proteolytic activity to cleave the synthetic SPP substrate, myc-Prl-PP-FLAG (31), suggesting that recombinant 3FSPP retained the proteolytic activity (see below). In fact, in agreement with previous results, photoaffinity probes based on transition state analog (Fig. 2*C*) as well as dipeptidic (DBZ-BpB3) (24) type inhibitors, all of which specifically targeted the endogenous SPP in mammalian cells (5, 24, 25), specifically labeled 3FSPP observed as a monomer band on SDS-PAGE. These data suggest that 3FSPP polypeptides overexpressed in Sf9 cells reconstituted the intramembrane-cleaving activity in a natural conformation.

We further purified the DDM-solubilized Sf9 cell lysates by affinity column using anti-FLAG antibody (Fig. 2*D*). Silver staining and immunoblot analysis of each fraction revealed that the major polypeptides in eluate fraction migrated at 50 and 100 kDa, corresponding to the monomer and the dimer of 3FSPP, respectively. Next we separated the purified 3FSPP by size-exclusion gel chromatography (SEC) (Figs. 2*E* and 3*A* and supplemental Fig. S2*A*). 3FSPP polypeptides were mainly detected at the fractions corresponding to ~250–450 kDa. Silver staining revealed that these fractions contained exclusively 3FSPP polypeptides. Moreover, all samples containing 3FSPP showed the SPP activity to cleave myc-Prl-PP-FLAG *in vitro*, suggesting that the high molecular weight complexes were composed only of proteolytically active 3FSPP (Fig. 2*F* and supplemental Fig. S2, *A* and *B*). The purified 3FSPP molecules were also subjected to BN-PAGE (Fig. 3*B*). DDM-solubilized 3FSPP was predominantly migrated as a 240-kDa high molecular mass complex similarly to endogenous SPP. In addition, 440- and 700-kDa complexes containing 3FSPP were detected. No additional major bands appeared between the 240-, 440-, and 700-kDa complexes, but three additional minor bands emerged below 240 kDa with an increased loading amount. Notably, these bands migrated as a monomer (60 kDa), dimer (120 kDa), and trimer (180 kDa) of 3FSPP, suggesting that the 240-kDa complex corresponds to a tetrameric complex of 3FSPP. Mutant
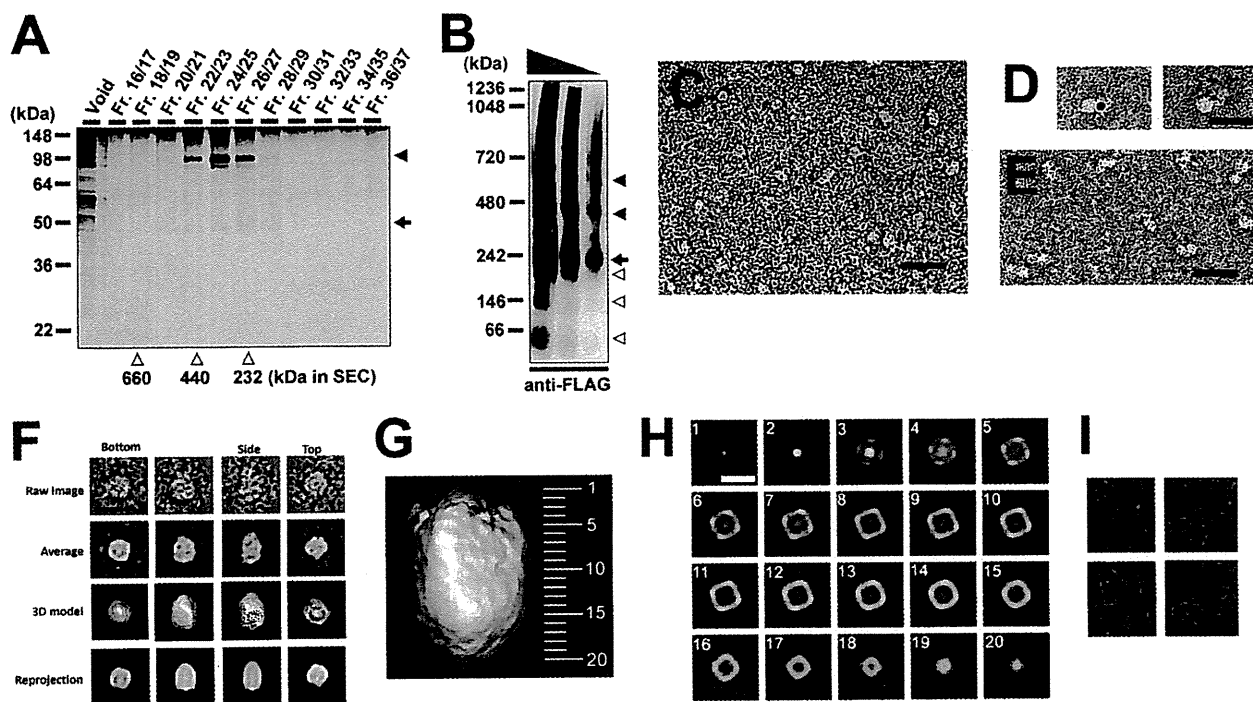
FIGURE 3. **Three-dimensional reconstruction of purified recombinant 3FSPP.** *A*, silver staining of affinity-purified 3FSPP separated by SEC. The *arrows* and *arrowheads* indicate the monomer and the dimer, respectively. Fractions (*Fr.*) containing SEC markers are represented by the *white arrowheads* below the *upper panel*. *B*, BN-PAGE analysis of affinity-purified 3FSPP. DDM-solubilized 3FSPP proteins were mainly detected as tetramers (*arrow*) and dimeric and trimeric tetramers (*black arrowheads*). Note that an increase in loading amount resulted in the appearance of the monomer, dimer, and trimer of 3FSPP (*white arrowheads*). *C*, electron microscopic observation of negatively stained fraction 27 in *panel A. Scale bar* represents 400 Å. *D*, electron microscopic observation of a negatively stained affinity-purified 3FSPP fraction coincubated with colloidal gold-conjugated anti-FLAG antibody. The *scale bar* represents 400 Å. *E*, electron microscopic observation of negatively stained fraction 21 in *panel A.* The *scale bar* represents 400 Å. *F*, raw images of SPP with different Euler angles (*row 1*) are compared with the corresponding two-dimensional averages (*row 2*), the surface views of the three-dimensional reconstruction (*row 3*), and the reprojections of the three-dimensional reconstruction (*row 4*) along the corresponding Euler directions. They are consistent through the reconstruction. The *scale bar* represents 100 Å. *G* and *H*, surface and sections of reconstructed 3FSPP. Horizontal slices perpendicular to the four-fold symmetric axis show the bullet-shaped molecule. Corresponding positions of the slices in *H* are numbered from 1 to 20 on the side view (*G*). The *scale bar* represents 100 Å. *I*, electron microscopic observation of the molecular complex of 3FSPP decorated with anti-FLAG antibody bound around the boat-tail domain. Contours are shown below.

3FSPP carrying the protease-inactive D219A mutation (6) was also detected as a 240-kDa complex on BN-PAGE, suggesting that SPP forms the high molecular mass complex irrespective of the enzymatic activity (supplemental Fig. S2C). These data suggest that active SPP was purified as a tetramer in the DDM-solubilized condition. Moreover, appearance of monomer and trimer species on BN-PAGE indicates that the tetrameric assembly is not a dimeric form of the SDS-resistant dimer. 440- and 700-kDa complexes may represent oligomeric forms of the tetramer (*i.e.* octamer and dodecamer, respectively). The sizes of DDM-solubilized native SPP (monomer, 45 kDa; complex, 200 kDa), dSPP (monomer, 40 kDa; complex, 180 kDa), and tagged SPPL2b (monomer, 90 kDa; complex, 400 kDa) are also consistent with tetramer formation, supporting the notion that the formation of a tetrameric complex is a common characteristic of the SPP family proteins.

Electron Microscopy and Three-dimensional Reconstruction of SPP—We then negatively stained the purified 3FSPP particles with uranyl acetate and viewed them by electron microscopy. In the fractions 26/27 (corresponding to 250 kDa from standard proteins) separated by SEC (Fig. 3, *A* and *B*), variously shaped particles of a uniform size were observed (Fig. 3*C*). These particles were labeled by colloidal gold-conjugated anti-

FLAG antibody, indicating the 3FSPP tetramer (Fig. 3*D*). The dimeric form of the particles, each of which also has the same dimensions, was observed in the 450-kDa fractions 20/21 of SEC (corresponding to 450 kDa from standards) (Fig. 3*E*), supporting the idea that the 440-kDa complex in BN-PAGE corresponds to the dimeric form of the 3FSPP tetramer. Most particles were rhomboid- or square-shaped with round corners (Fig. 3*C*). The variation in shape was interpreted to reflect different orientations of the same molecule on the grid. The square-shaped particles seemed to imply top views of the tetrameric form; the rhombuses would be side views. For three-dimensional reconstruction of the SPP molecule, image analysis was performed using our SPINNS program and IMAGIC V (33–37). The final reconstruction included 4,232 particles, 90.2% of all the selected images. Representative raw images are presented (Fig. 3*F, first row*), with their corresponding class averages (Fig. 3*F, second row*) and with surface representations and reprojections (Fig. 3*F, third* and *fourth rows*). Reprojections from the final volume are consistent with raw images and class averages, reflecting successful reconstruction from the original particle images. A plot of the Euler angles of the 117 adopted class averages (supplemental Fig. S3*A*) showed that SPP is almost randomly oriented on the grid surface.

According to the Fourier shell correlation (FSC) function (41), 22 Å, if FSC > 0.5, was used as the resolution criterion (supplemental Fig. S3B).

For surface representation, the three-dimensional map was contoured at an isosurface containing a volume corresponding to 327 kDa: 182% of the tetrameric SPP mass (179 kDa) calculated from the amino acid composition. The additional volume seems attributable to glycosylation (4, 12, 22) and the attached lipids and detergents. The surface representation depicts a bullet-shaped molecule with a pointed bottom tip and a boat-tail top (Fig. 3G). Viewed from the top, SPP is a square with round corners: 100×85 Å. The height estimated from the side views is 130 Å. The structure has four low density interior regions connected to exterior openings, which are capped by a plug-like structure at the top (Fig. 3H and supplemental Fig. S3C). Moreover, a cleft-like concave on the top of each rhomboid side connected to the large chamber was identified in the structure. Biochemical analyses revealed that SPP exposes N and C termini to the luminal and the cytosolic sides, respectively (42). To confirm the topology of the 3FSPP particle, purified 3FSPP was coincubated with anti-FLAG antibody and observed by electron microscopy. The particles were labeled with antibodies near the corners of the large domain (Fig. 3, D and I), suggesting that the boat-tail domain faces the luminal side and the tip locates at the cytosolic side. Taken together, single particle analysis revealed that the purified 3FSPP tetramer forms a bullet-shaped structure with an internal chamber.

N-terminal Region of SPP Is Responsible for Tetrameric Assembly—It was reported that the recombinant C-terminal region of SPP containing five transmembrane domains with the catalytic aspartates was able to reconstitute the substrate binding as well as proteolytic activity *in vitro* and was present as a monomer (43). We thus hypothesized that the remaining N-terminal half of SPP, which is the counterpart domain of the C terminus, is responsible for tetramer formation. To examine this, we first purified the N-terminal region of 3FSPP (3FSPP/NT; truncated human SPP (1–191 amino acids) fused with 3×FLAG tag at its N terminus) overexpressed in Sf9 cells (Fig. 4A and supplemental Fig. S4). In addition to a monomer (30 kDa), an SDS-resistant homodimer of 3FSPP/NT was detected similarly to the SPP holoprotein (Fig. 4B). Recombinant 3FSPP/NT polypeptides were also detected as 130- and 260-kDa complexes on BN-PAGE, corresponding to the tetramer and the dimeric tetramer, respectively (Fig. 4C). Purified 3FSPP/NT was also observed as a half-size particle of the 3FSPP holoprotein in negatively stained images (Fig. 4D). These data strongly suggested that the N-terminal region is a scaffold domain for the tetramer formation of SPP.

To examine the physiological relevance of the tetramer formation of SPP within cells, we overexpressed dSPP/NT, which encodes the truncated dSPP (1–200 amino acids) equivalent to human 3FSPP/NT (Fig. 5, A and B, and supplemental Fig. S4). Consistent with the putative scaffolding function observed in 3FSPP, overexpressed dSPP/NT was co-immunoprecipitated with endogenous dSPP (Fig. 5C). Next we analyzed the possible function of dSPP/NT using a chemical biology approach. SPP utilizes two functional sites
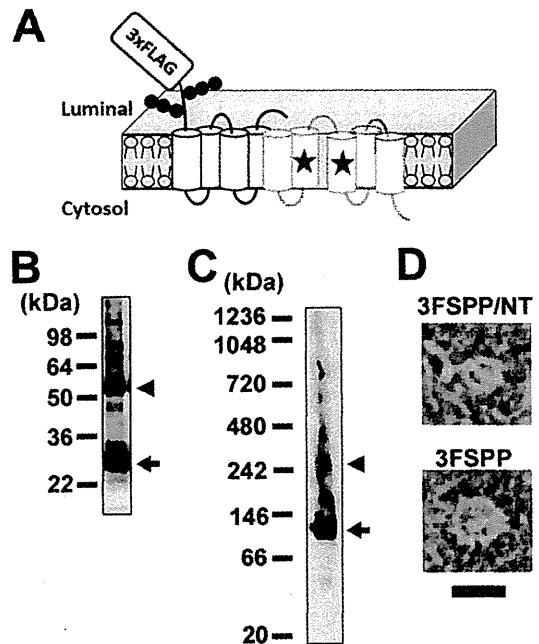

FIGURE 4. The N-terminal region of SPP is sufficient for tetrameric assembly. *A*, schematic depiction of 3FSPP/NT. *B*, immunoblot analysis of affinity-purified 3FSPP/NT by anti-FLAG antibody. The dimer and monomer forms of 3FSPP/NT are indicated by the *arrowhead* and *arrow*, respectively. *C*, affinity-purified 3FSPP/NT was analyzed using BN-PAGE in the DDM-solubilized condition. 3FSPP/NT proteins were mainly detected as tetramers (*arrow*) and dimeric tetramers (*arrowhead*). *D*, electron microscopic observation of negatively stained affinity-purified 3FSPP/NT as compared with 3FSPP. The *scale bar* represents 100 Å.

for the intramembrane cleavage, *i.e.* the initial substrate binding site and the catalytic site, which are directly targeted by the helical peptide- and the transition state analog-type inhibitors, respectively (8, 22, 31). A previous report indicated that both sites were present in the recombinant C-terminal fragment of dSPP (43). To test whether the dSPP/NT polypeptide harbors enzymatically functional sites, we performed a photoaffinity labeling experiment using the helical peptide- and the transition state analog-based photoprobes (pep.11-Bt and 31C-Bpa, respectively) (25, 44, 45). Consistent with the previous results, both wild-type dSPP and dSPP/D228A were labeled by pep.11-Bt, whereas 31C-Bpa was bound only to wild-type dSPP, suggesting that the initial substrate binding site was formed irrespective of the endoproteolytic activity of dSPP (Fig. 5D). However, no labeling of dSPP/NT was observed by either of the photoprobes, indicating that dSPP/NT does not harbor a functional site for the enzymatic activity. We then examined the effect of dSPP/NT overexpression on the proteolytic activity in cells. dSPP activity was detected by the transcriptional activation of the ERSE-driven firefly luciferase (26), which was mediated by specific intramembrane cleavage of the recombinant SPP substrate (SPP_{sub}) (22). We found that the coexpression of dSPP with ERSE reporter and SPP_{sub} in S2 cells increased luciferase activity, which was decreased by the coexpression of an aspartate mutant dSPP, suggesting that the reporter assay is applicable to dSPP in S2 cells similarly to mammalian cells. Intriguingly, the overexpression of dSPP/NT inhibited
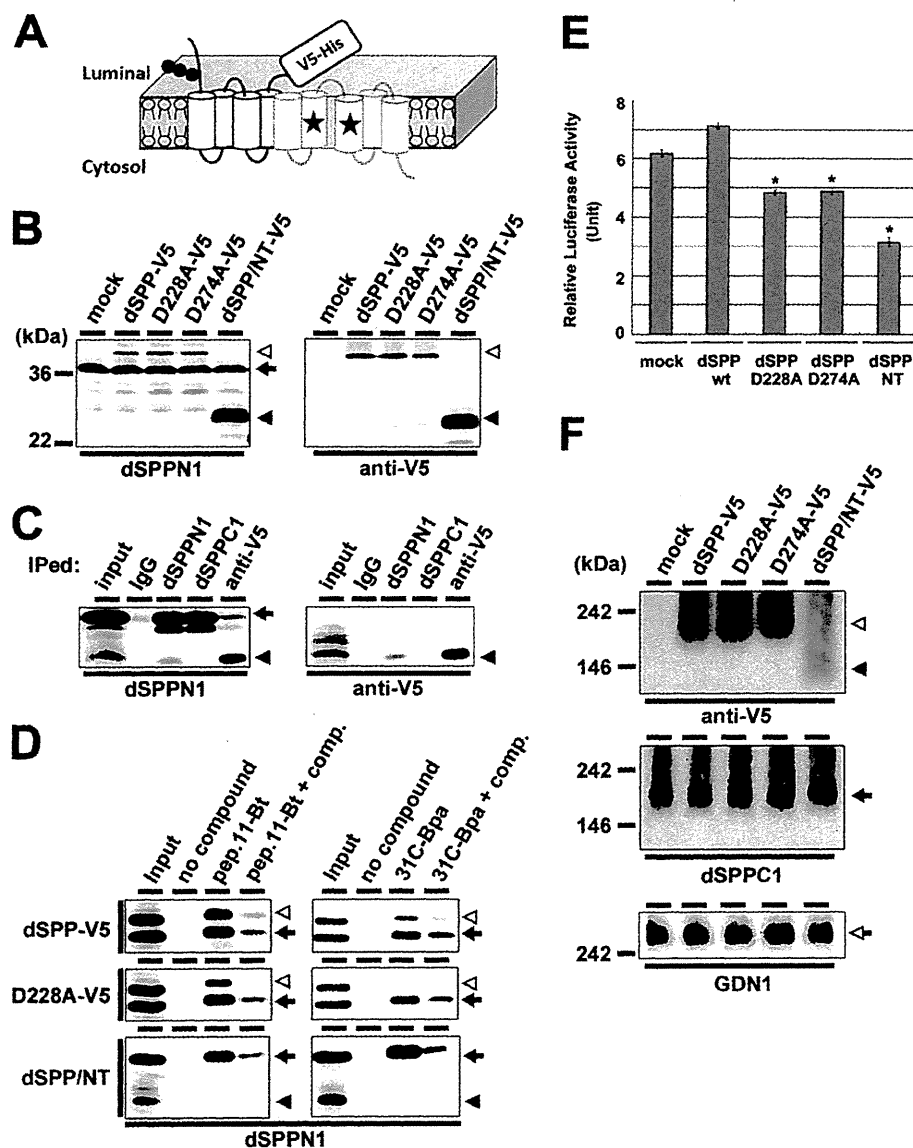
FIGURE 5. **Effect of the overexpression of dSPP/NT on enzymatic activity.** A, schematic depiction of dSPP/NT. B, immunoblot analysis of S2 cells expressing dSPP-V5 (*white arrowheads*) and dSPP/NT (*black arrowheads*). Endogenous dSPP is indicated by the *arrow*. C, immunoprecipitation of S2 cells expressing dSPP/NT. Endogenous dSPP and dSPP/NT are indicated by the *arrow* and *black arrowheads*, respectively. *IPed*, immunoprecipitated. D, photoaffinity labeling experiments using S2 cell lysates expressing wild-type dSPP, dSPP/D228A, or dSPP/NT. Endogenous and exogenous dSPP and dSPP/NT were shown by the *arrows*, *white arrowheads*, and *black arrowheads*, respectively. Note that coincubation with the parent compound (*comp.*; pep.11 for pep.11-Bt, 31C for 31C-Bpa) completely eliminated the labeling. E, cell-based dSPP activity assay using S2 cells expressing dSPP mutants ($n = 4$, mean $\pm$ S.E., *, $p < 0.05$, as compared with mock). F, the amount of dSPP tetramer in DDM-solubilized S2 cells expressing dSPP-V5 (*white arrowhead*) and dSPP/NT (*black arrowhead*) was analyzed by BN-PAGE. Endogenous dSPP is indicated by an *arrow* (*middle panel*). The levels of endogenous Psn polypeptides (*white arrow*) are used as a loading control (*lower panel*). Antibodies used are indicated below the lanes.

the proteolytic activity of endogenous dSPP in a similar manner to that observed by the expression of aspartate mutant dSPP, indicating that dSPP/NT functions as a dominant negative mutant (Fig. 5E). Moreover, the amount of the endogenous dSPP tetramer was reduced in cells expressing dSPP/NT (Fig. 5F). Considering that dSPP/NT lacked any mechanistically functional sites for enzymatic activity, interaction of dSPP/NT with the endogenous dSPP disrupted the tetrameric assembly, thereby causing the dominant negative effect. Collectively, these data suggest that the N-terminal region of SPP is responsible for the tetrameric assembly,

which might be the prerequisite for the intramembrane cleaving activity of SPP.

DISCUSSION

In this study, we analyzed the structure and biochemical character of SPP using *in vitro* as well as cell-based assays. We found that SPP forms a bullet-shaped tetramer with a large interior chamber. The tetrameric assembly was conserved among the SPP and SPP-like protease (SPPL) family proteins and was mediated by its N-terminal region. Overexpressed SPP/NT was incorporated into the SPP complex and inhibited

the enzymatic activity in living cells, implying that the tetramer formation is the prerequisite for the proteolytic activity of SPP.

It was reported that human SPP proteins formed a SDS-resistant dimer (40). In contrast to mammalian SPP proteins, dSPP was solely detected as a monomer in SDS-PAGE (Fig. 1B) (43). However, DDM-solubilized human SPP, SPPL2b, and dSPP polypeptides were mainly detected as a tetramer complex on BN-PAGE. Thus, the tetramer formation is mediated by a common molecular mechanism, and the binding mode of the tetramer should be distinct from the formation of the SDS-resistant dimer observed in human SPP or SPPL2b. SDS-resistant dimer formation is not a critical mechanistic feature; rather, it appears to be an artificial phenomenon in human SPP caused by SDS. We also found that the N-terminal half is sufficient for the tetrameric assembly of SPP, although the precise mode of interaction still remains unknown. However, SPP/ SPPL proteins were never cofractionated with other member proteins of the SPP family (19, 31), suggesting a specific mechanism of recognition and interaction behind homo-oligomerization. Very recently, 200-, 400-, and 600-kDa complexes containing SPP and its substrates were reported, in accordance with our results (46). EM showed a dimer form of the tetramer in SEC fractions 20 and 21, suggesting that the tetramer is an essential and minimal form of functional SPP. Further analyses will be needed to identify the critical domain(s) for the tetramerization.

A series of x-ray crystallographic studies revealed that the serine- and metalloprotease-types of I-CLiPs, e.g. rhomboid and S2P, respectively, harbor the active site residues within the hydrophilic cleft in the lipid bilayer (47). Moreover, we have biochemically shown that PS has the catalytic pore structure (48), suggesting that the hydrophilic interior structure of a catalytic site is a common feature essential to the intramembrane cleaving mechanism of I-CLiPs. Here, we analyzed the structure of SPP using single particle analysis and found that the SPP tetramer has a bullet-like structure with low density internal regions, to which the concaves near the boat-tail domain were connected. The boat-tail domain with its plug-like structure was predominantly labeled by an antibody targeting the N terminus, suggesting that SPP also has a hydrophilic chamber accessible from the luminal side (Fig. 6A). Intriguingly, the plug-like structure near the catalytic site was also predicted in the cytosolic side of PS (48). Considering the inverse topology of SPP as compared with PS (42), the four chambers within the SPP tetramer and the plug-like structures at the predicted luminal side represent the hydrophilic catalytic sites of SPP within the lipid bilayer, similarly to those of PS. The concaves connected to the chambers may represent the substrate entry sites. Furthermore, considering the previous study reporting that the C-terminal region of SPP restored proteolytic function in the monomeric state (43), we speculate that the N-terminal region functions as a scaffold for tetramer formation located at the center of the bullet-like structure. This may explain why a single anti-FLAG antibody bound to one tetramer despite high binding efficacy. Collectively, these data suggest that SPP forms a bullet-like tetramer with its N termini at the center, whereas the enzymatically active C terminus is located as an outer ring (Fig. 6B). Nevertheless, further fine structural analyses, e.g. single
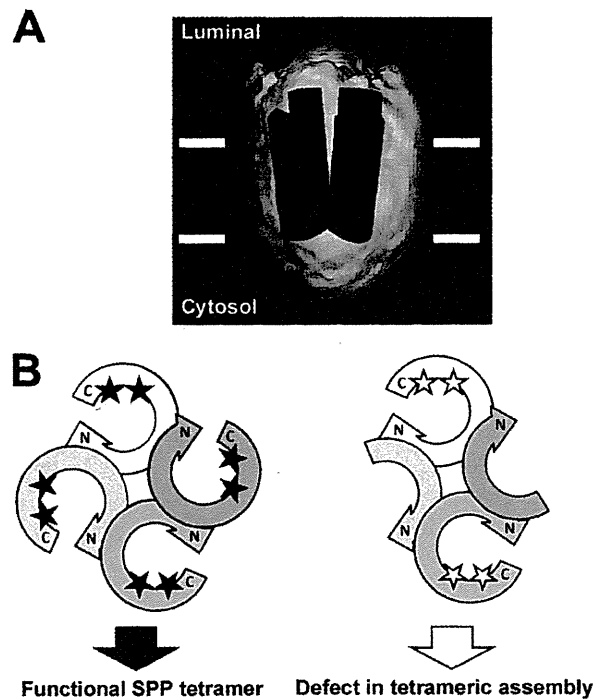
Functional SPP tetramer   **Defect in tetrameric assembly**

FIGURE 6. **Schematic depiction of three-dimensional structure of SPP.** *A,* illustration of putative topology and structure of catalytic chambers of reconstructed SPP. *B,* schematic diagram of SPP tetrameric complex (*left*). The *rounded arrow* represents a single SPP subunit. The *black stars* indicate the catalytically active aspartates. Incorporation of the N-terminal region with SPP (*right*) affected the tetramer formation (inactive catalytic sites were depicted as *white stars*) and resulted in a loss-of-function effect.

particle reconstruction using cryo-EM or x-ray crystallography, will be needed to clarify the precise structure and function relationships of SPP.

Overexpression of dSPP/NT inhibited the activity of endogenous dSPP similarly to that of the catalytic site mutant. In accordance with previous studies of the C-terminal region of SPP (43), our chemical biology approach revealed that dSPP/NT contains neither the initial substrate binding site nor the catalytic site, suggesting that the inhibitory effect of dSPP/NT is independent of the proteolytic machinery (*i.e.* defects in catalytic function or capturing of substrates). In addition, the possibility of a nonspecific hydrophobic interaction of the substrate with dSPP/NT was excluded because nonspecific labeling of dSPP/NT with photoprobes, including a highly hydrophobic helical peptide, was not detected. Rather, we found that the amount of dSPP tetramer was reduced in cells expressing dSPP/NT, which is capable of binding to the holoprotein, suggesting that the interaction of dSPP/NT affected the tetramer formation of the endogenous dSPP (Fig. 6B). These results are totally different from those observed with PS, which is a homologous protease; exogenous N- or C-terminal fragments (NTF or CTF, respectively) of PS failed to be incorporated into a functional complex, nor did it affect the levels or activity of endogenous γ-secretase (49, 50). Moreover, we failed to overexpress the C-terminal region of dSPP with or without dSPP/NT (data not shown), whereas the coexpression of PS NTF and CTF reconstituted the functional γ-secretase complex (51). Thus, the tetrameric assembly of SPP with its N-ter-

minal region is a unique feature of the SPP/SPPL family I-CLiPs. Oligomer formation is the prerequisite for the function of several channels, receptors, and transporters. In particular, the tetramer formation of aquaporin is critical to its water permeability and ion selectivity (52–54), whereas each aquaporin subunit has a water channel in the center. We speculate that the interaction of dSPP/NT resulted in a conformational change of each subunit that affects the formation and/or the stability of the dSPP tetramer, thereby causing the dominant negative effect (Fig. 6B). These results also imply that the N-terminal region is the scaffold domain for the formation of the enzymatically active SPP tetramer.

In sum, we have revealed that SPP forms a bullet-shaped tetramer with its N-terminal region in the proteolytically active state. However, we were not able to fully characterize the structure of SPP in the membrane-embedded state. Further fine structural analyses, *e.g.* reconstruction of SPP in the presence of lipids and x-ray analysis of its Type-I three-dimensional crystals composed of two-dimensional crystal layers in lipid, should eventually identify the mechanism by which the SPP complex recognizes the substrates, which in turn leads to the entrance of the substrates into the active site.

REFERENCES

1. Wolfe, M. S. (2009) *J. Biol. Chem.* **284**, 13969–13973
2. Fluhrer, R., Steiner, H., and Haass, C. (2009) *J. Biol. Chem.* **284**, 13975–13979
3. Golde, T. E., Wolfe, M. S., and Greenbaum, D. C. (2009) *Semin. Cell Dev. Biol.* **20**, 225–230
4. Weihofen, A., Binns, K., Lemberg, M. K., Ashman, K., and Martoglio, B. (2002) *Science* **296**, 2215–2218
5. Kornilova, A. Y., Das, C., and Wolfe, M. S. (2003) *J. Biol. Chem.* **278**, 16470–16473
6. Weihofen, A., Lemberg, M. K., Friedmann, E., Rueeger, H., Schmitz, A., Paganetti, P., Rovelli, G., and Martoglio, B. (2003) *J. Biol. Chem.* **278**, 16528–16533
7. Nyborg, A. C., Ladd, T. B., Jansen, K., Kukar, T., and Golde, T. E. (2006) *FASEB J.* **20**, 1671–1679
8. Sato, T., Ananda, K., Cheng, C. I., Suh, E. J., Narayanan, S., and Wolfe, M. S. (2008) *J. Biol. Chem.* **283**, 33287–33295
9. Edbauer, D., Winkler, E., Regula, J. T., Pesold, B., Steiner, H., and Haass, C. (2003) *Nat. Cell Biol.* **5**, 486–488
10. Kimberly, W. T., LaVoie, M. J., Ostaszewski, B. L., Ye, W., Wolfe, M. S., and Selkoe, D. J. (2003) *Proc. Natl. Acad. Sci. U.S.A.* **100**, 6382–6387
11. Takasugi, N., Tomita, T., Hayashi, I., Tsuruoka, M., Niimura, M., Takahashi, Y., Thinakaran, G., and Iwatsubo, T. (2003) *Nature* **422**, 438–441
12. Weihofen, A., Lemberg, M. K., Ploegh, H. L., Bogyo, M., and Martoglio, B. (2000) *J. Biol. Chem.* **275**, 30951–30956
13. Crawshaw, S. G., Martoglio, B., Meacock, S. L., and High, S. (2004) *Biochem. J.* **384**, 9–17
14. Loureiro, J., Lilley, B. N., Spooner, E., Noriega, V., Tortorella, D., and Ploegh, H. L. (2006) *Nature* **441**, 894–897
15. Martoglio, B., Graf, R., and Dobberstein, B. (1997) *EMBO J.* **16**, 6636–6645
16. Lemberg, M. K., Bland, F. A., Weihofen, A., Braud, V. M., and Martoglio, B. (2001) *J. Immunol.* **167**, 6441–6446
17. Grigorenko, A. P., Moliaka, Y. K., Soto, M. C., Mello, C. C., and Rogaev, E. I. (2004) *Proc. Natl. Acad. Sci. U.S.A.* **101**, 14955–14960
18. Casso, D. J., Tanda, S., Biehs, B., Martoglio, B., and Kornberg, T. B. (2005) *Genetics* **170**, 139–148
19. Krawitz, P., Haffner, C., Fluhrer, R., Steiner, H., Schmid, B., and Haass, C. (2005) *J. Biol. Chem.* **280**, 39515–39523
20. McLauchlan, J., Lemberg, M. K., Hope, G., and Martoglio, B. (2002) *EMBO J.* **21**, 3980–3988
21. Takasugi, N., Takahashi, Y., Morohashi, Y., Tomita, T., and Iwatsubo, T. (2002) *J. Biol. Chem.* **277**, 50198–50205
22. Nyborg, A. C., Jansen, K., Ladd, T. B., Fauq, A., and Golde, T. E. (2004) *J. Biol. Chem.* **279**, 43148–43156
23. Li, Y. M., Xu, M., Lai, M. T., Huang, Q., Castro, J. L., DiMuzio-Mower, J., Harrison, T., Lellis, C., Nadin, A., Neduvelil, J. G., Register, R. B., Sardana, M. K., Shearman, M. S., Smith, A. L., Shi, X. P., Yin, K. C., Shafer, J. A., and Gardell, S. J. (2000) *Nature* **405**, 689–694
24. Fuwa, H., Takahashi, Y., Konno, Y., Watanabe, N., Miyashita, H., Sasaki, M., Natsugari, H., Kan, T., Fukuyama, T., Tomita, T., and Iwatsubo, T. (2007) *ACS Chem. Biol.* **2**, 408–418
25. Imamura, Y., Watanabe, N., Umezawa, N., Iwatsubo, T., Kato, N., Tomita, T., and Higuchi, T. (2009) *J. Am. Chem. Soc.* **131**, 7353–7359
26. Yoshida, H., Haze, K., Yanagi, H., Yura, T., and Mori, K. (1998) *J. Biol. Chem.* **273**, 33741–33749
27. Hayashi, I., Urano, Y., Fukuda, R., Isoo, N., Kodama, T., Hamakubo, T., Tomita, T., and Iwatsubo, T. (2004) *J. Biol. Chem.* **279**, 38040–38046
28. Ogura, T., Mio, K., Hayashi, I., Miyashita, H., Fukuda, R., Kopan, R., Kodama, T., Hamakubo, T., Iwatsubo, T., Iwastubo, T., Tomita, T., and Sato, C. (2006) *Biochem. Biophys. Res. Commun.* **343**, 525–534
29. Morohashi, Y., Kan, T., Tominari, Y., Fuwa, H., Okamura, Y., Watanabe, N., Sato, C., Natsugari, H., Fukuyama, T., Iwatsubo, T., and Tomita, T. (2006) *J. Biol. Chem.* **281**, 14670–14676
30. Tomita, T., Maruyama, K., Saido, T. C., Kume, H., Shinozaki, K., Tokuhiro, S., Capell, A., Walter, J., Grünberg, J., Haass, C., Iwatsubo, T., and Obata, K. (1997) *Proc. Natl. Acad. Sci. U.S.A.* **94**, 2025–2030
31. Sato, T., Nyborg, A. C., Iwata, N., Diehl, T. S., Saido, T. C., Golde, T. E., and Wolfe, M. S. (2006) *Biochemistry* **45**, 8649–8656
32. Frank, J. (2006) *Three-Dimensional Electron Microscopy of Macromolecular Assemblies: Visualization of Biological Molecules in Their Native State*, Oxford University Press, New York
33. van Heel, M., Harauz, G., Orlova, E. V., Schmidt, R., and Schatz, M. (1996) *J. Struct. Biol.* **116**, 17–24
34. Ogura, T., and Sato, C. (2004) *J. Struct. Biol.* **146**, 344–358
35. Ogura, T., and Sato, C. (2004) *J. Struct. Biol.* **145**, 63–75
36. Ogura, T., and Sato, C. (2006) *J. Struct. Biol.* **156**, 371–386
37. Ogura, T., Iwasaki, K., and Sato, C. (2003) *J. Struct. Biol.* **143**, 185–200
38. Penczek, P., Radermacher, M., and Frank, J. (1992) *Ultramicroscopy* **40**, 33–53
39. Penczek, P. A., Grassucci, R. A., and Frank, J. (1994) *Ultramicroscopy* **53**, 251–270
40. Nyborg, A. C., Kornilova, A. Y., Jansen, K., Ladd, T. B., Wolfe, M. S., and Golde, T. E. (2004) *J. Biol. Chem.* **279**, 15153–15160
41. Harauz, G., and van Heel, M. (1986) *Optik* **73**, 146–156
42. Friedmann, E., Lemberg, M. K., Weihofen, A., Dev, K. K., Dengler, U., Rovelli, G., and Martoglio, B. (2004) *J. Biol. Chem.* **279**, 50790–50798
43. Narayanan, S., Sato, T., and Wolfe, M. S. (2007) *J. Biol. Chem.* **282**, 20172–20179
44. Das, C., Berezovska, O., Diehl, T. S., Genet, C., Buldyrev, I., Tsai, J. Y., Hyman, B. T., and Wolfe, M. S. (2003) *J. Am. Chem. Soc.* **125**, 11794–11795
45. Micchelli, C. A., Esler, W. P., Kimberly, W. T., Jack, C., Berezovska, O., Kornilova, A., Hyman, B. T., Perrimon, N., and Wolfe, M. S. (2003) *FASEB J.* **17**, 79–81
46. Schrul, B., Kapp, K., Sinning, I., and Dobberstein, B. (2010) *Biochem. J.* **427**, 523–534
47. Urban, S., and Shi, Y. (2008) *Curr. Opin. Struct. Biol.* **18**, 432–441

48. Sato, C., Morohashi, Y., Tomita, T., and Iwatsubo, T. (2006) *J. Neurosci.* **26,** 12081–12088
49. Tomita, T., Tokuhiro, S., Hashimoto, T., Aiba, K., Saido, T. C., Maruyama, K., and Iwatsubo, T. (1998) *J. Biol. Chem.* **273,** 21153–21160
50. Shirotani, K., Takahashi, K., and Tabira, T. (1999) *Neurosci. Lett.* **262,** 37–40
51. Laudon, H., Mathews, P. M., Karlström, H., Bergman, A., Farmery, M. R., Nixon, R. A., Winblad, B., Gandy, S. E., Lendahl, U., Lundkvist, J., and Näslund, J. (2004) *J. Neurochem.* **89,** 44–53
52. Mathai, J. C., and Agre, P. (1999) *Biochemistry* **38,** 923–928
53. King, L. S., Kozono, D., and Agre, P. (2004) *Nat. Rev. Mol. Cell Biol.* **5,** 687–698
54. Buck, T. M., Wagner, J., Grund, S., and Skach, W. R. (2007) *Nat. Struct. Mol. Biol.* **14,** 762–769

Comparison of Presenilin 1 and Presenilin 2 γ-Secretase Activities Using a Yeast Reconstitution System*[S]

Yoji Yonemura[‡], Eugene Futai[‡1], Sosuke Yagishita[‡], Satoshi Suo[‡], Taisuke Tomita[§], Takeshi Iwatsubo[§], and Shoichi Ishiura[‡2]

From the ‡Department of Life Sciences, Graduate School of Arts and Sciences, University of Tokyo, Tokyo 153-8902, Japan and the §Department of Neuropathology and Neuroscience, Graduate School of Pharmaceutical Sciences, University of Tokyo, Tokyo 113-0033, Japan

γ-Secretase is composed of at least four proteins, presenilin (PS), nicastrin (NCT), Aph1, and Pen2. PS is the catalytic subunit of the γ-secretase complex, having aspartic protease activity. PS has two homologs, namely, PS1 and PS2. To compare the activity of these complexes containing different PSs, we reconstituted them in yeast, which lacks γ-secretase homologs. Yeast cells were transformed with PS1 or PS2, NCT, Pen2, Aph1, and artificial substrate C55-Gal4p. After substrate cleavage, Gal4p translocates to the nucleus and activates transcription of the reporter genes ADE2, HIS3, and lacZ. γ-Secretase activity was measured based on yeast growth on selective media and β-galactosidase activity. PS1 γ-secretase was ~24-fold more active than PS2 γ-secretase in the β-galactosidase assay. Using yeast microsomes containing γ-secretase and C55, we compared the concentration of Aβ generated by PS1 or PS2 γ-secretase. PS1 γ-secretase produced ~24-fold more Aβ than PS2 γ-secretase. We found the optimal pH of Aβ production by PS2 to be 7.0, as for PS1, and that the PS2 complex included immature NCT, unlike the PS1 complex, which included mature NCT. In this study, we compared the activity of PS1 or PS2 per one γ-secretase complex. Co-immunoprecipitation experiments using yeast microsomes showed that PS1 concentrations in the γ-secretase complex were ~28 times higher than that of PS2. Our data suggest that the PS1 complex is only marginally less active than the PS2 complex in Aβ production.

γ-Secretase consists of at least four subunits, presenilin (PS),[3] nicastrin (NCT), anterior pharynx defective 1 (Aph1), and presenilin enhancer 2 (Pen2) (1). PS is the catalytic subunit of γ-secretase with aspartic protease activity (2, 3). Amyloid-β (Aβ) peptide, which plays a causative role in Alzheimer disease

(AD), is produced after sequential cleavage of amyloid-β precursor protein (APP) by β-secretase and γ-secretase. The Aβ mainly consists of Aβ40 and Aβ42 containing 40 and 42 amino acids, respectively. Aβ42 is more prone to aggregation (4) and more toxic to neuronal cells. Many studies have reported that familial AD (FAD) mutations in PS and APP result in increased ratios of Aβ42 to Aβ40. The high Aβ42 ratio is believed to lead to AD.

PS has two homologs, namely, PS1 and PS2 (67% identical at the amino acid level). Aph1 also has two homologs: Aph1a (with alternative splicing variants Aph1a-S and a-L) and Aph1b. Sato et al. (5) reported that γ-secretase contained only one of each subunit, and as such, six distinct γ-secretases exist. Indeed, both PS1 and PS2 form a γ-secretase complex with the other subunits, producing Aβ (6). γ-Secretase cleaves many type I transmembrane proteins including APP and Notch, but the mechanism by which the different γ-secretases select their substrates is unclear. These different γ-secretases may have different functions and substrate selectivity.

Ubiquitous expression of PS1 and PS2 mRNAs in many human and mouse tissues has been reported, with varying expression levels across their tissues and during brain development (7). For example, in human young adult and aged brains, PS1 and PS2 mRNAs expression was similar. The subcellular distribution of PSs are known to be predominantly in the endoplasmic reticulum and the Golgi compartment (8). Levitan et al. (9) showed that human PS1 and PS2 substituted for Caenorhabditis elegans sel-12, suggesting that PS1 and PS2 are functionally redundant.

Different phenotypes of PS1- and PS2-deficient mice have been reported. PS1 knock-out mice exhibit severe developmental defects and perinatal lethality (10, 11), whereas PS2 knockout mice show only mild phenotypes (12). Over 160 FAD mutations in PS1, but only 10 in PS2, have been found. These findings suggest that PS1 and PS2 play distinct roles in vivo.

Lai et al. (13) indicated that Ps1 (Ps, mouse presenilin) γ-secretase produced 169 times more Aβ than Ps2 γ-secretase, using membrane fractions from Ps1-(+/−), Ps2-(−/−), and Ps1-(−/−), Ps2-(+/+) blastocyst-derived cells from knock-out mice. In their study, γ-secretase activity was calculated as follows: level of produced Aβ/total Ps. They did not use the calculation: level of produced Aβ/Ps in γ-secretase complex and thus did not evaluate the active γ-secretase content.

Yagishita et al. (14) developed a novel γ-secretase assay using yeast microsomes. Yeast lacks endogenous γ-secretase and

Comparison of PS1 and PS2 γ-Secretase Activities

APP homologs, and one can reconstitute pure human γ-secretase in yeast and estimate the activity. Using this system, we compared the activity of PS1 and PS2 in γ-secretase complexes. Our data suggested that PS1-containing microsomes had much higher activity than PS2-containing microsomes. However, detailed analysis regarding the "active" γ-secretase complex revealed that the PS1 and PS2 complex produced similar levels of Aβ.

MATERIALS AND METHODS

Construction of γ-Secretase and Substrates—To reconstitute γ-secretase in yeast, human PS1 or PS2, NCT, Aph1a-L-HA, FLAG-Pen2, and substrates were cloned into the following vectors, as described previously (15). Briefly, PS1 or PS2 and NCT were ligated into KpnI and XbaI sites of the pBEVY-T vector (16). Aph1a-L-HA and FLAG-Pen2 were ligated into the XbaI and KpnI sites of pBEVY-L (16). C55-Gal4p, NotchTM-Gal4p, and C99 were fused to the *SUC2* signal sequence, facilitating translocation to the endoplasmic reticulum, and ligated into the BamHI and EcoRI sites of p426ADH (17). C55, C99, and NotchTM indicate amino acids 672–726 of the human APP770 isoform, 672–770 of the human APP770, 1703–1754 of the mouse Notch-1, respectively.

Myc-tagged PS1 and PS2 were PCR amplified and ligated into the KpnI site of pBEVY-T, using the following two pair of primers, respectively: mycPS1S, 5'-GGGGTACCAAAAA-TGGAACAAAAACTCATCTCAGAAGAGGATCTGATGA-CAGAGTTACCTGCACCGTTG-3' and PS1AS, 5'-GATC-CGCTTATTTAGAAGTGTCGAATTCGACCTCGGTACC-ATGCTAGATATAAAATTGATGGAATGC-3'; mycPS2S, 5'-GGGGTACCAAAAATGGAACAAAAACTCATCTCAG-AAGAGGATCTGATGCTCACATTCATGGCCTCTGAC-3' and PS2AS, 5'-GGGGTACCTCAGATGTAGAGCTGA-TGGGAGG-3'.

Yeast Transformation—Three plasmids were transformed into *Saccharomyces cerevisiae* strain PJ69–4A (*MATa, trp1–901, leu2-3, 112, ura3-52, his3-200, gal4Δ, gal80Δ, LYS2::GAL1-HIS3, GAL2-ADE2, met2::GAL7-lacZ*) (18). The transformants were selected on SD media plate lacking Leu, Trp, and Ura (SD-LWU). In microsome assays, we used the yeast strain PJ69–4Apep4Δ(*MATa, trp1–901, leu2-3, 112, ura3-52, his3-200, gal4Δ, gal80Δ, LYS2::-GAL1-HIS3, GAL2-ADE2, met2::GAL7-lacZ, pep4::kanMX*) (14) to avoid endogenous protease activity.

Reporter Gene Expression—Expression of *HIS3* (His) and *ADE2* (Ade) was estimated by transformant growth on SD-LWHUAde. β-Galactosidase assays were performed as described previously (15). Transformants were cultured in SD-LWU media until they reached an A_{600} of ~0.8. Cells were collected after centrifugation and suspended in lysis buffer (20 mM Tris-Cl (pH 8.0), 10 mM MgCl₂, 50 mM KCl, 1 mM EDTA, 5% glycerol, 1 mM dithiothreitol) including protease inhibitor mixture (Sigma), and lysed by glass beads. Protein concentration and β-galactosidase activity of the cell lysates were determined.

γ-Secretase Assay and Immunoblotting—Using yeast microsomes, we detected Aβ using an in vitro γ-secretase assay. *In vitro* γ-secretase assays were performed as described previ-

ously, with minor modifications (14). Microsomes (80 μg) were solubilized with γ-buffer (50 mM MES (pH 5.5) or 50 mM PIPES (pH 6.0, 6.5, 7.0, 7.5), or 50 mM HEPES (pH 8.0), 250 mM sucrose, 1 mM EGTA) containing 1% CHAPSO on ice for 60 min. Inhibitor mixture, thiorphan, *O*-phenanthroline, CHAPSO, and γ-buffer were added to the solubilized microsomes, as described previously (14). The mixture was incubated at 37 °C for 0 or 24 h. After incubation, the sample was extracted with chloroform/methanol (2:1) followed by addition of sample buffer, and boiled at 100 °C for 5 min. Aβ production was analyzed by Western blotting using the specific antibody, 82E1. Band signal was quantified using an LAS-3000 luminescent image analyzer (FujiFilm, Tokyo, Japan).

Immunoprecipitation of γ-Secretase—Microsomes (400 μg) were solubilized with IP buffer containing 1% CHAPSO and protease inhibitor mixture, on ice, for 60 min. Solubilized membranes were added to 40 μl of anti-FLAG affinity gel (50% slurry) (Sigma) and rotated at 4 °C for 2 h. Beads were washed with IP buffer and suspended in sample buffer containing 8 M urea to prepare the "IP sample" from 400 μg of microsomes. The "input sample" was prepared as follows: 100 μl of sample buffer containing 8 M urea was added to 80 μg of microsomes and incubated at 65 °C for 10 min. Microsomes (8 μg, 10–11 μl) were loaded as input.

Antibodies—The following antibodies were used for immunoblotting: monoclonal antibodies against Aβ, 82E1 (IBL, Fujioka, Japan), HA (12CA5; Sigma), FLAG (M2; Sigma), and polyclonal antibodies against NCT (AB5890; Chemicon, Temecula, CA), Myc, 2272 (Cell Signaling Technology, Beverly, MA), the PS1 loop region (G1L3) (19), and the PS2 loop region (G2L) (20).

RESULTS

PS2 Was Less Active than PS1 in Growth and β-Galactosidase Assays—We constructed recombinant plasmids for γ-secretase and APP-based (C55-Gal4p) or Notch-based substrates (NotchTM-Gal4p) (15). We introduced the vectors into yeast strain PJ69, which expresses *HIS3, ADE2*, and *lacZ* under Gal4p control, and generated yeast transformants expressing the γ-secretase subunits (PS1 or PS2, NCT, Aph1a-L-HA, FLAG-Pen2) and an artificial substrate (C55-Gal4p or NotchTM-Gal4p). Gal4p released from C55-Gal4p or NotchTM-Gal4p by reconstituted γ-secretase activates *HIS3* and *ADE2* genes transcription. Therefore, γ-secretase activity was assessed by growth on media lacking histidine and adenine. As a result, yeast expressing PS1 γ-secretase and C55-Gal4p could replicate on the selection media. Yeast expressing PS2 γ-secretase could also grow, but was much slower than that of PS1-expressing yeast (Fig. 1A). PS1 L166P, G384A, and PS2 N141I are familial Alzheimer disease (FAD) mutations. Yeast carrying these mutations were unable to grow on media lacking histidine and adenine. After isolating these yeast cell lysates, we measured β-galactosidase activity to estimate γ-secretase activity. PS1 had ~24 times more β-galactosidase activity than PS2 (Fig. 1B). The results of the β-galactosidase assay were well correlated with the growth assay results (Fig. 1, A and B).

Next, we used NotchTM-Gal4p as a substrate instead of C55-Gal4p. The results were similar to those obtained when using
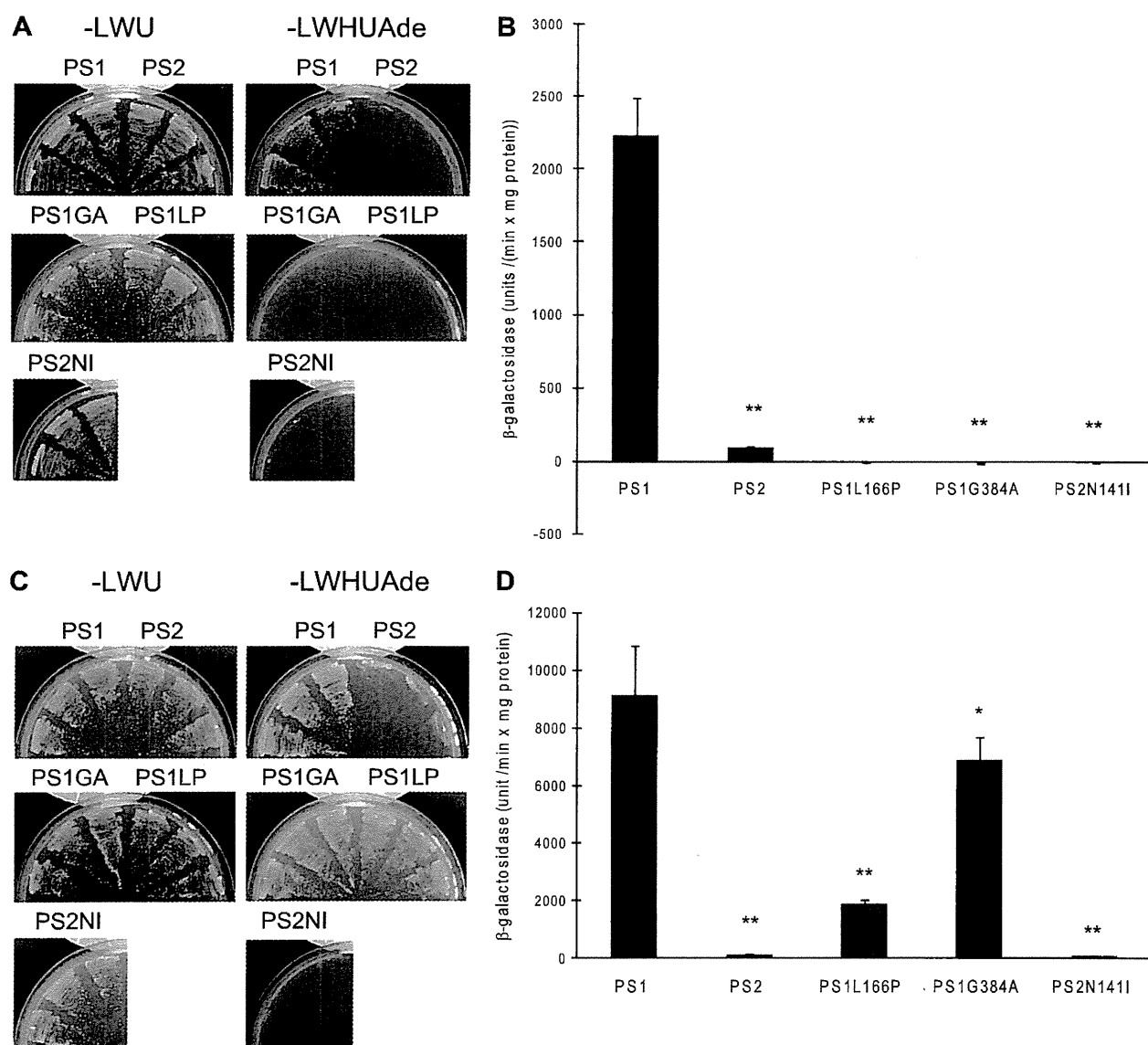
FIGURE 1. **Estimate of reconstituted PS1 or PS2 γ-secretase activity in yeast.** *A* and *C*, yeast cells were transformed with PSs (PS1 or PS2, or PS with FAD mutations), NCT, FLAG-Pen2, Aph1a-L-HA, and C55-gal4p (*A*), or NotchTM-gal4p (*C*). Three independent clones were cultured on non-selection media (SD-LWU) or selection media (SD-LWHUAde) at 30 °C for 3 days. Yeast cells not expressing PS did not grow on SD-LWHUAde. *B* and *D*, β-galactosidase activity was measured for each yeast lysate. Lysates were prepared from yeast cells using glass beads. One unit of β-galactosidase activity corresponds to 1 nmol of *O*-nitrophenyl β-d-galactopyranoside hydrolyzed per min, and activity was calculated as unit/(min × mg of protein in lysate). The activity was normalized by subtracting the activity in the absence of PS, 65 unit/(min × mg protein). Data are presented as mean value ± S.D., $n = 18$ (*A*), $n = 3$ (*C*) *, $p < 0.05$; **, $p < 0.01$ (analyzed by one-way analysis of variance followed by Dunnett's multiple comparison test). Statistical analyses were performed with PRISM software.

the C55-Gal4p, with the following two exceptions. Notch1 was more likely to be cleaved by γ-secretase than C55 (APP) (Fig. 1, *B versus D*) and yeast cells expressing PS1 with FAD mutations (L166P and G384A) were able to grow on SD-LWHUAde, whereas cells expressing PS2 N141I were not (Fig. 1*D*). These results suggested that PS1 with the FAD mutations cannot cleave APP, whereas they can cleave Notch like wild-type γ-secretase.

Optimal pH for Aβ Production by the PS2 Complex—To study γ-secretase activity *in vitro*, we prepared yeast microsomes from yeast transformants expressing PS1 or PS2, NCT, Aph1a-L-HA, FLAG-Pen2, and C55 (14). Three previous reports showed that γ-secretase with PS1 maximally

produced Aβ at approximately pH 7.0 (14, 21, 22). The optimum pH of Aβ production by γ-secretase with PS2, however, remains unclear. Thus, we investigated the optimal pH of the PS2 complex to produce Aβ. When yeast microsomes prepared from three independent clones were incubated for 24 h at 37 °C with 0.25% CHAPSO and 0.1% PC, we found that the PS2 complex also maximally produced Aβ at approximately pH 7.0 in all three assays (Fig. 2, *A* and *B*), suggesting that the PS1 and PS2 complex have similar pH dependences for Aβ production.

Levels of Aβ Production by PS1 or PS2—We compared the level of Aβ produced by PS1 or PS2 using yeast microsomes. Each microsome was incubated at 37 °C for 24 h in the pres-

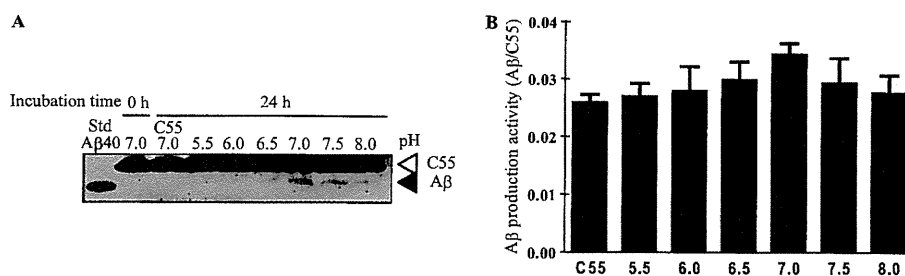# Comparison of PS1 and PS2 γ-Secretase Activities

A

B

FIGURE 2. **Optimum pH of Aβ production by PS2.** *A,* microsomes (80 μg) prepared from three independent yeast cells transformed with PS2, NCT, Aph1a-L-HA, FLAG-Pen2, and C55, and from yeast expressing C55 were incubated with 0.25% CHAPSO and 0.1% PC at 37 °C for 0 or 24 h. Incubation samples were subjected to immunoblotting to compare Aβ production activity, Aβ/C55. Aβ was detected by 82E1. Synthetic Aβ40 (20 pg) was used as a positive control. Yeast expressing C55 and microsomes incubated for 0 h were loaded as a negative control. *B,* three independent assays were quantified using analyzing software (LAS-3000 luminescent image analyzer, Fuji Film, Tokyo, Japan). The column represents the mean ± S.D. (*n* = 3).
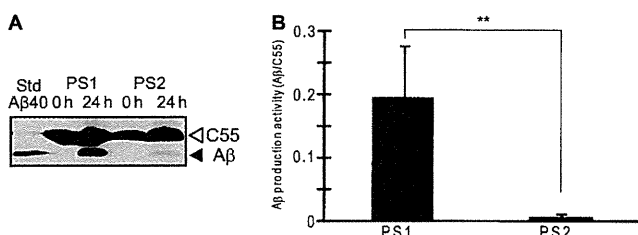
A

B

FIGURE 3. **Difference in Aβ production between PS1 and PS2.** *A,* yeast microsomes expressing PS1 or PS2, NCT, Aph1a-L-HA, FLAG-Pen2, and C55 were subjected to *in vitro* γ-secretase assays at pH 7.0. Aβ produced by PS1 or PS2 γ-secretase was detected. Synthetic Aβ40 (30 pg) was loaded as a marker. *B,* the bands obtained in *A* were quantified to determine the ratio of Aβ to C55 using analyzing software (LAS-3000 luminescent image analyzer, Fuji Film, Tokyo, Japan). The column represents the mean ± S.D. (*n* = 5, **, *p* < 0.01). Data were analyzed by Student's *t* test.

ence of 0.25% CHAPSO and 0.1% PC. We found that the PS1 complex produced significantly more Aβ than PS2 (Fig. 3*A*). By quantifying the Western blotting signals, we calculated that PS1 produced ∼24 times more Aβ than PS2 (Fig. 3*B*).

PS1 Complexes Were More Abundant than PS2 Complexes— To verify whether PS, NCT, Aph1a-L, and Pen2 form the γ-secretase complex, we isolated membrane fractions from yeast introduced with PS, NCT, Aph1a-L-HA, FLAG-Pen2, and C99, and performed co-immunoprecipitation experiments with the anti-FLAG M2 affinity gel. Both PS1 and PS2 were co-immunoprecipitated with FLAG-Pen2 (Fig. 4, *B* and *C*). NCT and Aph1a-L were also co-immunoprecipitated with FLAG-Pen2 (Fig. 4*A*), suggesting that PS1 and PS2 formed a γ-secretase complex. We also found that the PS2 complex predominantly included non-glycosylated immature NCT, whereas the PS1 complex contained highly glycosylated mature NCT (Fig. 4*A*).

Comparison of the PS1 and PS2 contents in γ-secretase is difficult due to the variable affinity of their specific antibodies. To estimate the amount of PS1 or PS2 in γ-secretase complexes, we constructed Myc-tagged PS1 and PS2. We introduced these constructs into yeast and reconstituted the γ-secretases. Preparing these microsomes, we immunoprecipitated γ-secretase complexes with anti-FLAG affinity gel. The immunoprecipitates were next subjected to immunoblotting. Aph1a-L levels in the PS1 or PS2 complex were similar (Fig. 5*A*). The Myc-tagged PS1 complex included mainly mature NCT, while Myc-tagged PS2 complexes contained immature NCT (Fig. 5*A*). The level of PS1 NTF in γ-secretase complexes

(associated with FLAG Pen2) was ∼28 times higher than that of PS2 NTF (Fig. 5*B*).

When calculating γ-secretase activity per one γ-secretase complex from these data, a significant difference between PS1 and PS2 does not exist. However, the PS1 complex was 24.15 more active in the β-galactosidase assay. *In vitro* Aβ production assays indicated that PS1 was 24.61 more active than PS2. Comparing PS1 and PS2 contents in γ-secretase in a co-immunoprecipitation experiment, we found that the amount of PS1NTF in the γ-secretase complex was 28.14 times higher than that of PS2NTF. These data suggested that the complete PS2 complex was 1.142 or 1.143 times more active than the PS1 complex.

DISCUSSION

γ-Secretase assays measuring released Aβ into conditioned media from cultured cells have been previously performed. These assays found that γ-secretase with PS FAD mutations increased the Aβ 40/42 ratio. However, very few *in vitro* assays have been reported. To accurately study γ-secretase activity, Yagishita *et al.* (14) established an *in vitro* assay system using yeast, which possesses no γ-secretase homologs. This system enabled us to directly compare activities between the PS1 and PS2 complex.

Yeast growth and β-galactosidase assays using C55-Gal4p or Notch-Gal4p as a substrate revealed that PS1 had a significantly higher activity than PS2. We also found that FAD mutations in PS abolished APP processing activity, and that PS1 L166P and G384A cleaved Notch with reduced activity compared with wild-type PS1. The assembly of PS1 FAD mutants (L166P or G384A) into γ-secretase complex was also assessed by immunoprecipitation (supplemental Fig. S1). The assembly of PS1 L166P mutant was similar to PS1 WT. On the other hand, ∼36% of PS1 G384A (comparing to the WT) formed the γ-secretase complex. These results showed that PS1 L166P assembled normally with defective protease activity and PS1 G384A was defective both in the assembly and the protease activity, suggesting that loss of function of PS caused lower cleavage activity. These reductions in processing activity obtained in this report support PS loss of function hypothesis, which is believed to cause FAD (23). We evaluated the activity of other PS1 FAD mutations (A79V, M146L, A231V, M233T, and ΔExon9) in Notch cleavage (data not shown). Our Notch
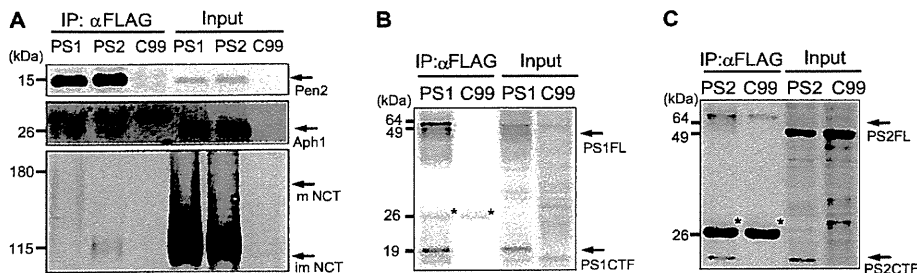
FIGURE 4. **Formation of PS1 and PS2 γ-secretase complexes.** Yeast microsomes expressing PS1 or PS2, NCT, Aph1a-L-HA, FLAG-Pen2, and C99, and microsomes expressing C99 were solubilized with IP buffer containing 1% CHAPSO and protease inhibitor mixture. γ-Secretase complexes were immunoprecipitated with anti-FLAG affinity gel (Sigma). The immunoprecipitates and input fraction were subjected to immunoblotting. NCT, Aph1, Pen2, and PS were detected by specific antibodies. The *asterisks* indicate nonspecific bands.
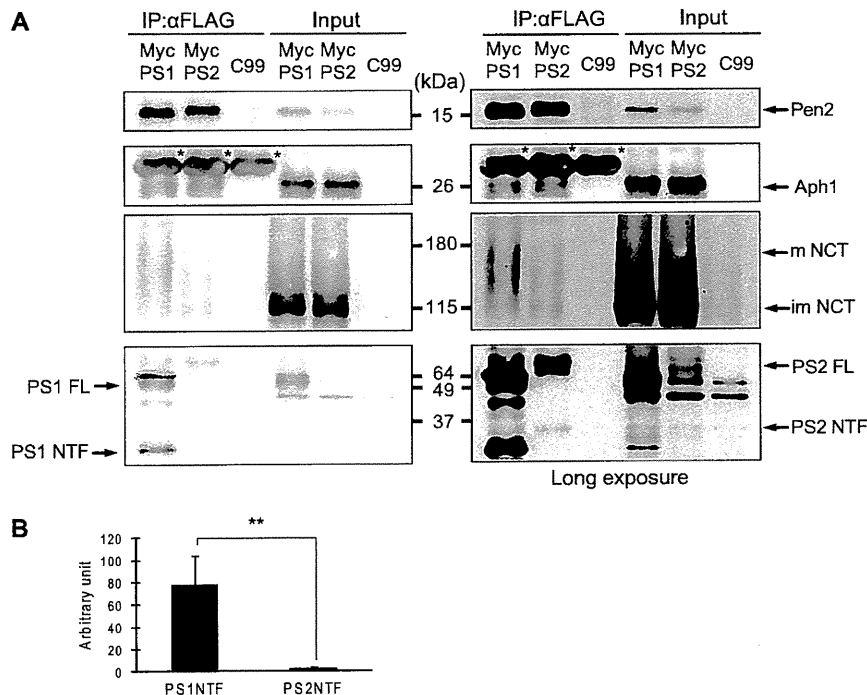

FIGURE 5. **Quantification of PS1 and PS2 in γ-secretase complexes.** A, yeast expressing Myc-tagged PS1 or PS2, the other secretase subunits, and C99, were incubated with anti-FLAG affinity gel. The immunoprecipitates were analyzed by immunoblotting. B, amount of Myc-tagged PS1NTF and Myc-tagged PS2NTF in the γ-secretase complexes were quantified using LAS-3000 luminescent image analyzer (Fuji Film, Tokyo, Japan). Data were analyzed by Student's t test. Error bar shows the mean ± S.D. $n = 4$, **, $p < 0.01$. The *asterisks* indicate nonspecific bands.

cleavage results with PS1 FAD mutations, PS1L166P and G384A, corroborated the findings of earlier studies (24, 25).

Based on the *in vitro* γ-secretase assay using yeast microsomes, we found that γ-secretase with PS2 optimally produced Aβ at approximately pH 7.0. Previous reports have shown that PS1 also maximally produced Aβ at pH 7.0 (14, 21, 22), suggesting that PS1 and PS2 make Aβ using a similar mechanism.

Our co-immunoprecipitation experiments using yeast microsomes containing PS1 or PS2, NCT, Aph1a-L-HA, and FLAG-Pen2 showed that PS2 bound to immature NCT, whereas PS1 bound to the mature NCT. Expression levels of immature or mature NCTs in cells transformed with PS1 or PS2 were similar, but the anti-FLAG affinity gel immunoprecipitates contained different levels of immature and mature NCT. Frånberg *et al.* (26) reported that Ps2 bound to immature NCT in Ps1-deficient (Ps1-(−/−), Ps2-(+/+)) MEF cells and Ps1 bound to mature NCT in Ps2 deficient (Ps1-(+/+), Ps2-(−/−))

MEF cells using affinity capture with an active site-directed γ-secretase inhibitor. This difference in NCT maturation in the complex may affect substrate affinity.

In this study, we used Aph1a-L as a γ-secretase subunit, which may facilitate PS2 binding to immature NCT. Also, Aph1a-S expression, or Aph1b as a γ-secretase subunit, may result in alternative binding patterns, such as PS2 binding to mature NCT or PS1 binding with immature NCT. In fact, we observed the PS1 complex with Aph1a-S containing more immature NCT than the PS1 complex with Aph1a-L (data not shown). To date, γ-secretase is known to target many substrates, but how γ-secretase selects its substrates is unclear. These variable γ-secretases may contribute to specific substrate selection.

To compare the γ-secretase activity of PS1 and PS2 precisely, we employed two different approaches. First, we used C55(-Gal4p) or C99 as a substrate instead of C100Flag. NCT

plays a role in binding to the substrate by recognizing N terminus of C99 (27). So, natural N terminus of C99 or C55 is important to assess γ-secretase activity correctly. Using C100Flag as a substrate may result in inaccurate evaluation, because C100Flag possesses one extra amino acid, methionine, on the N terminus. Second, we estimated the amount of PS1 or PS2 in the γ-secretase complex. Lai *et al.* (13) reported Ps1 and Ps2 γ-secretase activity as a function of total protein concentration, but not all PS localizes to the γ-secretase complex. Therefore, γ-secretase activity should be calculated as follows: γ-secretase activity/concentration of PS in γ-secretase complex. γ-Secretase assembly is not a random process, but occurs sequentially. NCT and Aph1 form the NCT-Aph1 subcomplex in the initial step of complex formation. Two hypotheses have been proposed regarding the subsequent steps in γ-secretase complex assembly. One hypothesis is that PS binds to the NCT-Aph1 subcomplex, followed by Pen2, creating a γ-secretase complex (28, 29). Alternatively, the PS-Pen2 intermediate may bind to the preexisting NCT-Aph1 subcomplex to form the γ-secretase complex (30). To evaluate the construction process of the γ-secretase complex, we compared PS1 or PS2 in the γ-secretase complex by co-immunoprecipitating Myc-tagged PS1 or PS2 with anti-FLAG antibody (FLAG tag is on Pen2). Co-immunoprecipitation with other antibodies detecting NCT, Aph1, or PS could lead to inaccurate estimates regarding the amount of Myc-PS in the γ-secretase complex. We found that the concentration of PS2 in the γ-secretase complex was much lower than that of PS1. Because we applied a minimal reconstitution system in yeast, unknown protein(s) may stabilize PS2. This possibility is currently being explored.

In this study, we reconstituted human PS1 and PS2 γ-secretase complexes and compared their Aβ production (per γ-secretase complex). PS1 had 24.65 times and 24.61 times higher activity than PS2 in the β-galactosidase and *in vitro* Aβ production assay, respectively. Based on Co-IP experiments, the amount of PS1 in the γ-secretase complex was 28.14 times higher than that of PS2. Thus, our data suggest that PS1 did not have significantly higher activity than PS2, as has been reported (13). PS1 and PS2 were 67% identical at the amino acid level, suggesting that these two proteins have related functions in the γ-secretase complex. Our results suggest that the difference between PS1 and PS2 is their affinity to the other γ-secretase subunits. The contribution of PS1 on γ-secretase activity is more important than that of PS2 because PS1 knock-out mice exhibit severe phenotypes, whereas PS2 knock-out mice do not. We hypothesize that the differences in PS1 and PS2 knock-out mice phenotypes may result from different amounts of PS1 and PS2 γ-secretases, but not differences in their activity.

Currently, PS1 is believed to have a higher activity than PS2 in γ-secretases, while we showed that they have similar activities. In corroboration of our findings, recent reports have shown that PS2 γ-secretase cleaved more APP than PS1 γ-secretase in microglia cells, regardless of the presence of PS1 (31). Thus, when studying γ-secretase activity, we should consider the concentration of PS in the active γ-secretase complex, which may aid in clarifying the pathogenesis of FAD caused by PS loss-of-function FAD mutations.

REFERENCES

1. Edbauer, D., Winkler, E., Regula, J. T., Pesold, B., Steiner, H., and Haass, C. (2003) *Nat. Cell Biol.* **5,** 486–488
2. Wolfe, M. S., Xia, W., Ostaszewski, B. L., Diehl, T. S., Kimberly, W. T., and Selkoe, D. J. (1999) *Nature* **398,** 513–517
3. Steiner, H., Duff, K., Capell, A., Romig, H., Grim, M. G., Lincoln, S., Hardy, J., Yu, X., Picciano, M., Fechteler, K., Citron, M., Kopan, R., Pesold, B., Keck, S., Baader, M., Tomita, T., Iwatsubo, T., Baumeister, R., and Haass, C. (1999) *J. Biol. Chem.* **274,** 28669–28673
4. Jarrett, J. T., and Lansbury, P. T., Jr. (1993) *Cell* **73,** 1055–1058
5. Sato, T., Diehl, T. S., Narayanan, S., Funamoto, S., Ihara, Y., De Strooper, B., Steiner, H., Haass, C., and Wolfe, M. S. (2007) *J. Biol. Chem.* **282,** 33985–33993
6. Shirotani, K., Tomioka, M., Kremmer, E., Haass, C., and Steiner, H. (2007) *Neurobiol. Dis.* **27,** 102–107
7. Lee, M. K., Slunt, H. H., Martin, L. J., Thinakaran, G., Kim, G., Gandy, S. E., Seeger, M., Koo, E., Price, D. L., and Sisodia, S. S. (1996) *J. Neurosci.* **16,** 7513–7525
8. Zhang, J., Kang, D. E., Xia, W., Okochi, M., Mori, H., Selkoe, D. J., and Koo, E. H. (1998) *J. Biol. Chem.* **273,** 12436–12442
9. Levitan, D., Doyle, T. G., Brousseau, D., Lee, M. K., Thinakaran, G., Slunt, H. H., Sisodia, S. S., and Greenwald, I. (1996) *Proc. Natl. Acad. Sci. U.S.A.* **93,** 14940–14944
10. Shen, J., Bronson, R. T., Chen, D. F., Xia, W., Selkoe, D. J., and Tonegawa, S. (1997) *Cell* **89,** 629–639
11. Wong, P. C., Zheng, H., Chen, H., Becher, M. W., Sirinathsinghji, D. J., Trumbauer, M. E., Chen, H. Y., Price, D. L., Van der Ploeg, L. H., and Sisodia, S. S. (1997) *Nature* **387,** 288–292
12. Herreman, A., Hartmann, D., Annaert, W., Saftig, P., Craessaerts, K., Serneels, L., Umans, L., Schrijvers, V., Checler, F., Vanderstichele, H., Baekelandt, V., Dressel, R., Cupers, P., Huylebroeck, D., Zwijsen, A., Van Leuven, F., and De Strooper, B. (1999) *Proc. Natl. Acad. Sci. U.S.A.* **96,** 11872–11877
13. Lai, M. T., Chen, E., Crouthamel, M. C., DiMuzio-Mower, J., Xu, M., Huang, Q., Price, E., Register, R. B., Shi, X. P., Donoviel, D. B., Bernstein, A., Hazuda, D., Gardell, S. J., and Li, Y. M. (2003) *J. Biol. Chem.* **278,** 22475–22481
14. Yagishita, S., Futai, E., and Ishiura, S. (2008) *Biochem. Biophys. Res. Commun.* **377,** 141–145
15. Futai, E., Yagishita, S., and Ishiura, S. (2009) *J. Biol. Chem.* **284,** 13013–13022
16. Miller, C. A., 3rd, Martinat, M. A., and Hyman, L. E. (1998) *Nucleic Acids Res.* **26,** 3577–3583
17. Mumberg, D., Müller, R., and Funk, M. (1995) *Gene* **156,** 119–122
18. James, P., Halladay, J., and Craig, E. A. (1996) *Genetics* **144,** 1425–1436
19. Tomita, T., Takikawa, R., Koyama, A., Morohashi, Y., Takasugi, N., Saido, T. C., Maruyama, K., and Iwatsubo, T. (1999) *J. Neurosci.* **19,** 10627–10634
20. Tomita, T., Tokuhiro, S., Hashimoto, T., Aiba, K., Saido, T. C., Maruyama, K., and Iwatsubo, T. (1998) *J. Biol. Chem.* **273,** 21153–21160
21. Li, Y. M., Lai, M. T., Xu, M., Huang, Q., DiMuzio-Mower, J., Sardana, M. K., Shi, X. P., Yin, K. C., Shafer, J. A., and Gardell, S. J. (2000) *Proc. Natl. Acad. Sci. U.S.A.* **97,** 6138–6143
22. Fraering, P. C., Ye, W., Strub, J. M., Dolios, G., LaVoie, M. J., Ostaszewski, B. L., van Dorsselaer, A., Wang, R., Selkoe, D. J., and Wolfe, M. S. (2004) *Biochemistry* **43,** 9774–9789
23. Shen, J., and Kelleher, R. J., 3rd (2007) *Proc. Natl. Acad. Sci. U.S.A.* **104,** 403–409
24. Steiner, H., Kostka, M., Romig, H., Basset, G., Pesold, B., Hardy, J., Capell, A., Meyn, L., Grim, M. L., Baumeister, R., Fechteler, K., and Haass, C.

(2000) *Nat. Cell Biol.* **2**, 848–851

25. Moehlmann, T., Winkler, E., Xia, X., Edbauer, D., Murrell, J., Capell, A., Kaether, C., Zheng, H., Ghetti, B., Haass, C., and Steiner, H. (2002) *Proc. Natl. Acad. Sci. U.S.A.* **99**, 8025–8030

26. Frånberg, J., Svensson, A. I., Winblad, B., Karlström, H., and Frykman, S. (2011) *Biochem. Biophys. Res. Commun.* **404**, 564–568

27. Shah, S., Lee, S. F., Tabuchi, K., Hao, Y. H., Yu, C., LaPlant, Q., Ball, H., Dann, C. E., 3rd, Südhof, T., and Yu, G. (2005) *Cell* **122**, 435–447

28. LaVoie, M. J., Fraering, P. C., Ostaszewski, B. L., Ye, W., Kimberly, W. T.,

Wolfe, M. S., and Selkoe, D. J. (2003) *J. Biol. Chem.* **278**, 37213–37222

29. Niimura, M., Isoo, N., Takasugi, N., Tsuruoka, M., Ui-Tei, K., Saigo, K., Morohashi, Y., Tomita, T., and Iwatsubo, T. (2005) *J. Biol. Chem.* **280**, 12967–12975

30. Fraering, P. C., LaVoie, M. J., Ye, W., Ostaszewski, B. L., Kimberly, W. T., Selkoe, D. J., and Wolfe, M. S. (2004) *Biochemistry* **43**, 323–333

31. Jayadev, S., Case, A., Eastman, A. J., Nguyen, H., Pollak, J., Wiley, J. C., Möller, T., Morrison, R. S., and Garden, G. A. (2010) *PloS One* **5**, e15743

Neurobiology of Disease

BACE1 Activity Is Modulated by Cell-Associated Sphingosine-1-Phosphate

Nobumasa Takasugi,[1,3,4] Tomoki Sasaki,[1] Kunimichi Suzuki,[1] Satoko Osawa,[1] Hayato Isshiki,[1] Yukiko Hori,[1] Naoaki Shimada,[2] Takuya Higo,[2] Satoshi Yokoshima,[2] Tohru Fukuyama,[2] Virginia M.-Y. Lee,[5,6] John Q. Trojanowski,[5,6] Taisuke Tomita[1,4] and Takeshi Iwatsubo[1,3,4]

Departments of [1]Neuropathology and Neuroscience and [2]Synthetic Natural Products Chemistry, Graduate School of Pharmaceutical Sciences, and [3]Department of Neuropathology, Graduate School of Medicine, The University of Tokyo, Bunkyo-ku, Tokyo 113-0033, Japan, [4]Core Research for Evolutional Science and Technology, Japan Science and Technology Corporation, Bunkyo-ku, Tokyo 113-0033, Japan, and [5]Alzheimer's Disease Core Center and [6]Department of Pathology and Laboratory Medicine, University of Pennsylvania School of Medicine, Philadelphia, Pennsylvania 19104

Sphingosine kinase (SphK) 1 and 2 phosphorylate sphingosine to generate sphingosine-1-phosphate (S1P), a pluripotent lipophilic mediator implicated in a variety of cellular events. Here we show that the activity of β-site APP cleaving enzyme-1 (BACE1), the rate-limiting enzyme for amyloid-β peptide (Aβ) production, is modulated by S1P in mouse neurons. Treatment by SphK inhibitor, RNA interference knockdown of SphK, or overexpression of S1P degrading enzymes decreased BACE1 activity, which reduced Aβ production. S1P specifically bound to full-length BACE1 and increased its proteolytic activity, suggesting that cellular S1P directly modulates BACE1 activity. Notably, the relative activity of SphK2 was upregulated in the brains of patients with Alzheimer's disease. The unique modulatory effect of cellular S1P on BACE1 activity is a novel potential therapeutic target for Alzheimer's disease.

Introduction

Amyloid-β peptide (Aβ) is the major component of senile plaques deposited in the brains of patients with Alzheimer's disease (AD). Several lines of evidence suggest that the accumulation of Aβ is linked to the pathogenesis of AD (Tomita, 2009; De Strooper et al., 2010). Aβ is derived from amyloid-β precursor protein (APP) that is sequentially cleaved by two aspartate proteases, β- and γ-secretases. The major β-secretase is a type-1 transmembrane protein termed BACE1 (β-site APP cleaving enzyme 1) (Vassar et al., 2009). BACE1-deficient mice do not generate Aβ (Cai et al., 2001; Luo et al., 2001), but they exhibited hypomyelination (Hu et al., 2006; Willem et al., 2006) and altered neurological phenotype (Laird et al., 2005; Savonenko et al., 2008; Hu et al., 2010). However, modest reduction of BACE1

activity is sufficient for a significant reduction in brain Aβ deposition in AD model mice (McConlogue et al., 2007; Chow et al., 2010). Moreover, several reports indicate that the protein levels and/or the activity of BACE1 were increased in the brains of patients with sporadic AD (Fukumoto et al., 2002; Yang et al., 2003; Li et al., 2004; Ahmed et a., 2010), suggesting that subtle changes in BACE1 activity significantly impact on the pathomechanism of AD. BACE1 resides in the lipid raft, a membrane microdomain enriched in cholesterol and sphingolipids, and a significant role of lipids and microdomain is implicated in the regulation of the β-cleavage (Kalvodova et al., 2005; Rajendran et al., 2008; Vetrivel and Thinakaran, 2010). In this study, we focused on a biologically active lipid metabolite, sphingosine-1-phosphate (S1P). S1P functions as a ligand for G-protein-coupled receptor (GPCR)-type receptors from the extracellular side; alternatively, S1P has been shown to directly act on intracellular targets (Alvarez et al., 2007; Takabe et al., 2008; Pyne and Pyne, 2010). S1P is produced by phosphorylation of sphingosine by two related rate-limiting kinases, sphingosine kinase 1 (SphK1) and SphK2 (see Fig. 1A). Although SphK1 and SphK2 show different kinetic properties and tissue expression patterns (Blondeau et al., 2007; Spiegel and Milstien, 2007), both kinases are functionally redundant in the production of S1P in vivo (Mizugishi et al., 2005). Here, we show that modulation of SphK and S1P degrading enzymes alters the Aβ generation by regulating the β-cleavage via direct action of S1P on BACE1 protein. Furthermore, we found that SphK2 activity is increased in the brains of patients with sporadic AD. These data unveil a novel regulatory mechanism of BACE1 linked to S1P levels in neurons, supporting the view that SphK2/S1P is a novel potential therapeutic target for AD.
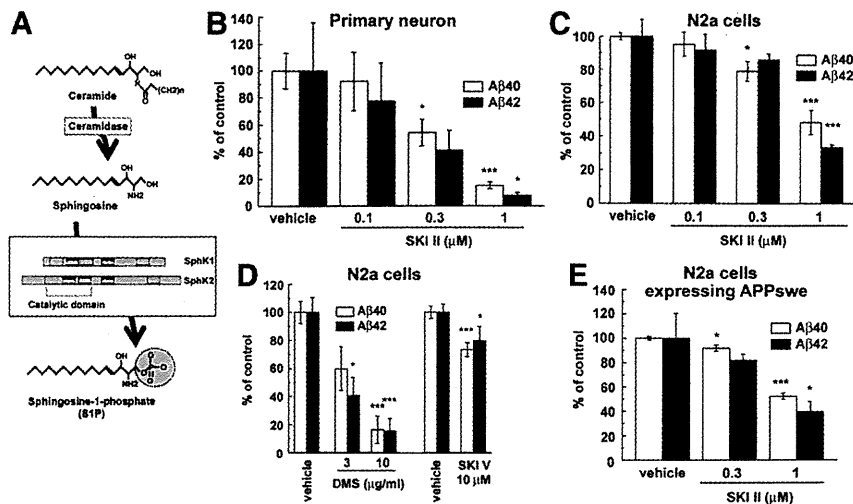
Figure 1. Sphingosine kinase inhibitors decreased the $A\beta$ secretion from neuronal cells. **A**, Schematic depiction of synthetic pathway for S1P. Five conserved regions of SphK are indicated by rectangles. Location of catalytic region is also indicated in this diagram. **B–E**, Effects of SKI on secretion of $A\beta_{40}$ and $A\beta_{42}$ from neuronal cells. The levels of secreted $A\beta$ in conditioned media were quantified by ELISAs. Mean $\pm$ SEM percentages of the relative ratio of secreted $A\beta$ to levels in untreated control are indicated. $*p < 0.05$, $***p < 0.001$ by Student's t test. **B**, Levels of secreted $A\beta$ from mouse primary cortical neurons (7 d *in vitro*) after treatment with SKI II for 24 h ($n = 4$). **C**, Levels of secreted $A\beta$ from N2a cells after treatment with SKI II for 24 h ($n = 4$). **D**, Levels of secreted $A\beta$s from N2a cells after treatment with DMS or SKI V for 24 h ($n = 4–7$). **E**, Levels of secreted $A\beta$ measured by human $A\beta$-specific ELISA from N2a cells stably expressing Swedish mutant of APP after treatment with SKI II for 24 h ($n = 4$).

Figure 2. SKI II decreased the β-secretase cleavage products. **A–D**, Immunoblot analyses of the protein levels of APP derivatives and BACE1 in neuronal cells. Immunoblot analysis of cell lysates (**A**) and cultured media (**B**) of mouse primary cortical neurons (7 d *in vitro*) treated with BACE inhibitor IV (BSI IV; 1 μM) or SKI II (1 μM) for 24 h in duplicate ($n = 3$; representative results are shown). Immunoblot analysis of cell lysates (**C**) and cultured media (**D**) of naive N2a cells treated with BACE inhibitor IV (BSI IV; 1 μM) or SKI II (3 μM) for 24 h. **E**, Levels of secreted human $A\beta$ from N2a cells overexpressing SC100 after treatment with SKI II for 24 h. Secreted human $A\beta_{40}$ and $A\beta_{42}$ were detected by human $A\beta$-specific ELISA ($n = 4$; mean $\pm$ SEM). **F**, Effect of SKI II (1 μM) on the cell-surface levels of APP in naive N2a cells. After treatment with vehicle or SKI II for 24 h, N2a cells were biotinylated by sulfo-NHS-biotin and pulled down by streptavidin beads.

Materials and Methods

Compounds. N-[N-(3,5-Difluorophenacetyl)-L-alanyl]-(S)-phenylglycine t-butyl ester (DAPT) was synthesized as described previously (Kan et al., 2003). ABC294640 [3-(4-chlorophenyl)-adamantane-1-carboxylic acid (pyridin-4-ylmethyl)amide] was synthesized according to the reported procedure (U.S. Patent 2006287317). Sphingosine kinase inhibitor (SKI) II (Sigma-Aldrich), SKI V (Sigma-Aldrich), N,N-dimethyl-sphingosine (DMS) (Cayman Chemical), β-secretase inhibitor IV (Calbiochem), S1P (Calbiochem), and 2-acetyl-4-tetrahydroxybutylimi-dazole (THI) (Matreya) were purchased from the indicated vendors. DAPT, β-secretase inhibitor IV, SKI II, and SKI V were dissolved in DMSO, DMS were dissolved in ethanol, and S1P was dissolved in 3 mM NaOH. Lipid immobilized aga-rose beads were purchased from Echelon. Synthetic $A\beta_{1-42}$ peptides (Peptide Institute) were solubilized at a concentration of 0.6 mg/ml in PBS and incubated at 37°C for 24 h to form $A\beta$ fibrils (Hori et al., 2007).

Antibodies and immunological methods. PS1 C-terminal fragment (CTF) (G1L3) was raised as described previously (Tomita et al., 1999). The following antibodies were purchased from the indicated vendors: human $A\beta$ 82E1 (catalog #10323; Immuno-Biological Laboratories), APP (18) (catalog #28053; Immuno-Biological Laboratories), BACE1 (c) (catalog #18711; Immuno-Biological Laboratories), APP (c) (catalog #18961; Immuno-Biological Laboratories), anti-mouse/rat APP (597) (catalog #28055; Immuno-Biological Laboratories), anti-BACE1 (42) (catalog #28051; Immuno-Biological Laboratories), anti-sAPPβwt (catalog #18957; Immuno-Biological Laboratories), SphK2 (P-19) (SC-22704; Santa Cruz Biotechnology), TRAF2 (C-20) (SC-876; Santa Cruz Biotechnology), SphK1 (catalog #10006822; Cayman Chemical), α-Tubulin DM1A (T9026; Sigma-Aldrich), α-actin AC-40 (A4700; Sigma-Aldrich), anti-βIII-tubulin Tuj1 (MAB1195; R & D Systems), APP N-terminal 22C11 (MAB348; Millipore), and anti-Myc 9B11 (catalog #2276; Cell Signaling Technology). The samples were analyzed by immunoblotting or two-site ELISAs for the detection of $A\beta$ as described previously (Iwatsubo et al., 1994; Tomita et al., 1997). For immunoblot detection for sAPPα and sAPPβ in cultured media, anti-human/mouse APP (597) and anti-sAPPβwt antibodies were used. Specificities of APP antibodies were shown previously (Fukumoto et al. 2010). For lipid binding assay, naive Neuro-2a (N2a) cell lysates or recombinant BACE1 [corresponding to its extracellular domain with a 10×His tag (catalog #931AS; R & D Systems)] were solubilized with 40 mM HEPES buffer, pH 7.4, containing 150 mM NaCl, 0.5% NP-40, and Complete protease inhibitor cocktail (Roche Applied Science) and spun down. Supernatants were coincubated with the lipid coated beads (Echelon Biosciences) or Nickel-NTA beads (Qiagen) that were preincubated with 3% BSA in HEPES buffer. After 3 h, bound proteins were eluted by sample buffer and subjected to immunoblotting.

Cell culture and transfection. Expression constructs for human APP carrying Swedish mutation (APPNL), SC100, and NΔE were described previously (Kopan et al., 1996; Tomita et al., 1997). cDNAs encoding SphK2, S1P phosphatase (SGPP1), and S1P lyase (SGPL1) were inserted into pcDNA3.1DV5–His/TOPO (Invitrogen) and mutant cDNAs were generated by long PCR-based Quikchange strategy (Stratagene). All constructs were sequenced using Thermosequenase (GE Healthcare) on an automated Sequencer (Li-Cor). N2a cells are maintained as described (Tomita et al., 1997). Primary cortical neurons were prepared from BALB/c mice at embryonic day 16 and grown in Neurobasal medium supplemented with B27 (Invitrogen) for 7 d (Fukumoto et al., 1999). Plasmid transfection was performed using Lipofectamine2000 (Invitro-
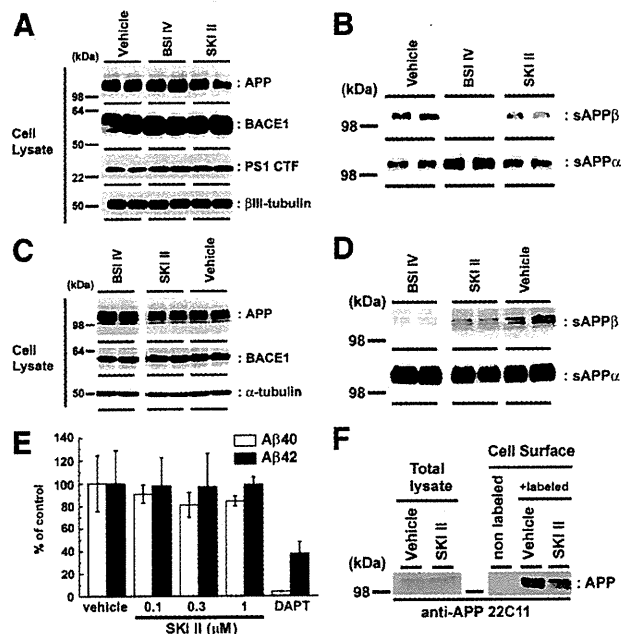
gen) or Fugene 6 (Roche Applied Science) following the instructions of the manufacturer. Small interfering RNA (siRNA) duplexes targeting to control, mouse *Sphk1* and *Sphk2* (target sequences: *Sphk1*, 5'-CTG GAC CAG TTG CAT ATA GAA-3'; *Sphk2*, 5'-TAG GCC TGG CCT CGT TGC ATA-3') were purchased from Qiagen. Each siRNA was reversely transfected in N2a cells using LipofectAMINE RNAiMax (Invitrogen) following the instructions of the manufacturer.

In vitro *secretase activity assay*. For in vitro β-secretase assay, recombinant human BACE1 (catalog #931AS; R & D Systems) or cell membranes of N2a, primary neuronal cells, or mouse brain (Hashimoto et al., 2002; Takasugi et al., 2003) were used as enzyme sources. After homogenization in 10 mM Tris, pH 7.0, the enzyme fractions were acidified by 25 mM CH₃COONa, pH 4.5, and incubated with the β-secretase-specific substrate JMV2236 (Bachem) at 37°C at the indicated times. Fluorescence of the fractions was measured at 320 and 420/430 nm as excitation and emission wavelengths, respectively. In vitro α-secretase assay was performed using SensoLyte 520 TACE (α-Secretase) Activity Assay kit (Anaspec) following the instructions of the manufacturer. N2a cells were treated with the indicated reagent for 24 h and collected cell membrane. Ten micrograms of protein were used as enzymatic source, and reaction were performed for 30 min.

In vitro *SphK2 activity assay*. Specific SphK2 activity assay was performed according to a previous report (Zemann et al., 2006; Don et al., 2007). After 48 h incubation, cells were washed with iced PBS and lysed by freeze–thaw cycle in 50 mM HEPES, pH 7.4, 10 mM KCl, 15 mM MgCl₂, 0.1% Triton X-100, 20% glycerol, 2 mM orthovanadate, 2 mM dithiothreitol, 10 mM NaF, 1 mM deoxypyridoxine, and EDTA-free complete protease inhibitor (Roche Applied Science). Lysates were cleared by centrifugation at 15,000 rpm for 5 min. The lysates and NBD-Sphingosine (10 μM final; Avanti Polar Lipids) were mixed in the reaction buffer (50 mM HEPES, pH 7.4, 15 mM MgCl₂, 0.5 mM KCl, 10% glycerol, and 2 mM ATP) and incubated for 30 min at 30°C. The reactions were stopped by the addition of equal amount of 1 M potassium phosphate, pH 8.5, followed by addition of 2.5-fold chloroform/methanol (2:1), and then centrifuged at 15,000 rpm for 1 min. Only the reactant NBD-S1P, but not the substrate NBD-Sphingosine, was collected in alkaline aqueous phase. After aqueous phase was combined with an equal amount of dimethylformamide, the fluorescence value was read. For the analysis of human brains, Tris-soluble fractions were used as an enzyme source. Specificity of this method has been described previously (Zemann et al., 2006).

SKI II treatment in wild-type and AD model mice. All experiments using animals in this study were performed according to the guidelines provided by the Institutional Animal Care Committee of the Graduate School of Pharmaceutical Sciences, The University of Tokyo. All animals were maintained on food and water with a 12 h light/dark cycle. Wild-type female mice (C57BL; SLC Japan) at 8 weeks of age were used. SKI II was dissolved at 2 μM in 40% DMSO/PBS. Each 2 μl solution was administered by stereotaxic injection into the hippocampus (bregma −2.6 mm, 3.1 mm lateral, 2.4 mm depth). After 8 h, the hippocampus of injected and uninjected site were isolated. Hippocampus samples were solubilized with 10 mM Tris buffer containing 1% 3-[(3-cholamidopropyl)dimethylammonio]-1-propanesulfonate and subjected to the sandwich ELISA for Aβ (Wako Chemical). A7 transgenic mice overexpress human APP695 harboring K670N, M671L, and T714I FAD mutations in neurons under the control of Thy1.2 promoter (Yamada et al., 2009). Female A7 mice at 6 months of age were used for subchronic treatment of SKI II. SKI II was dissolved in corn oil and injected orally for 7 d (50 mg·kg⁻¹·d⁻¹).

Human brain samples. Human brain samples from AD and aged control patients were derived from tissue bank at the University of Pennsylvania Alzheimer's Disease Core Center (ADCC) and the Center for Neurodegenerative Disease Research (CNDR). Control and AD brains were diagnosed symptomatically and pathologically at ADCC–CNDR as described (Arnold et al., 2010). All samples used for experimental measures were derived from frontal cortex under approval by the institutional review board, ADCC–CNDR, and institutional ethical committee of Graduate School of Pharmaceutical Sciences, The University of Tokyo. Brain samples were homogenized in TSI buffer (50 mM Tris HCl, pH 7.6, 150 mM NaCl, 0.5 mM diisopropyl fluorophosphate, 0.5 mM phenylmethylsulfonyl fluoride, 1 mM EGTA, 1 mg/ml antipain, 1 mg/ml leupeptin, 1 mg/ml pepstatin, 1 mg/ml Na-p-tosyl-L-lysine chloromethyl ketone) and
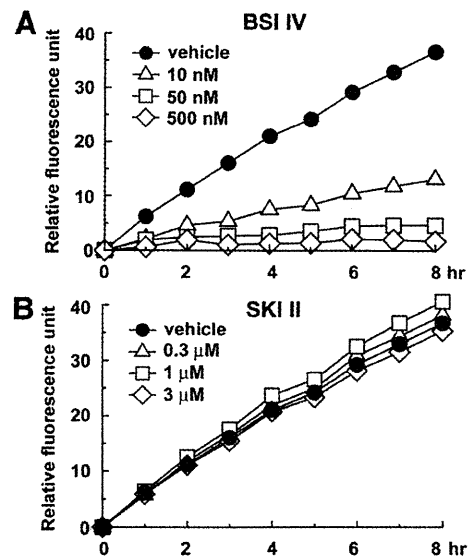

Figure 3. Effect of SKI II on the catalytic activity of BACE1. In vitro BACE1 activity assay using a fluorogenic BACE1-specific substrate. BACE inhibitor IV (BSI IV; A) or SKI II (B) was coincubated with recombinant soluble BACE1 protein at indicated duration and concentrations. Relative fluorescence units were shown (n = 3).

centrifuged at 260,000 × *g* for 20 min. Supernatant was collected as Tris-soluble fraction and used for SphK assay.

Results

SphK inhibitors decreased Aβ secretion by reducing the β-cleavage of APP

To investigate the relationship between S1P and Aβ production, we focused on the activity of SphKs (Fig. 1A). Recently, several small compounds that specifically inhibit SphKs have been developed as anti-cancer drugs (Pyne and Pyne, 2010). Treatment with a SphK-selective inhibitor, SKI II (French et al., 2003, 2006), decreased the secretion of endogenous Aβ from mouse primary cortical neurons (Fig. 1B), as well as in mouse neuroblastoma N2a cells, in a dose-dependent manner (Fig. 1C). Two additional selective SphK inhibitors with different chemical structure (i.e., N,N-dimethylsphingosine and SKI V) also decreased the Aβ secretion from N2a cells (Fig. 1D). SKI II treatment decreased the Aβ secretion from N2a cells overexpressing the Swedish mutant form of human APP (APPNL) (Fig. 1E). These data suggest an inhibitory effect of SphK inhibitors on Aβ secretion. Notably, both Aβ₄₀ and Aβ₄₂ levels were affected in a similar manner in all following experiments. Next we analyzed the APP metabolism in SKI II-treated cells. SKI II treatment did not affect the expression levels of either BACE1 or presenilin-1, which is the γ-secretase catalytic component, in primary cortical neuron (Fig. 2A) or N2a cells (Fig. 2B), respectively. Because the treatment of authentic BACE1 inhibitor IV abolished the secretion of β-secretase-mediated cleavage product of APP, i.e., sAPPβ, in conditioned media, SKI II treatment also caused a moderate but significant decrease in sAPPβ in primary cortical neurons (Fig. 2C) or N2a cells (Fig. 2D). In contrast, SKI II showed no effect on the cleavage of the C-terminal stub of human APP (SC100) that serves as a direct substrate of γ-secretase (Fig. 2E). Moreover, SKI II treatment caused neither an increase in in vitro α-secretase activity in cell membranes (78.9 ± 2.3% compared with DMSO treatment, n = 4) nor change in the level of APP on the plasma membrane (Fig. 2F). Collectively, these data strongly suggest that SKI II directly affected the β-cleavage of APP.
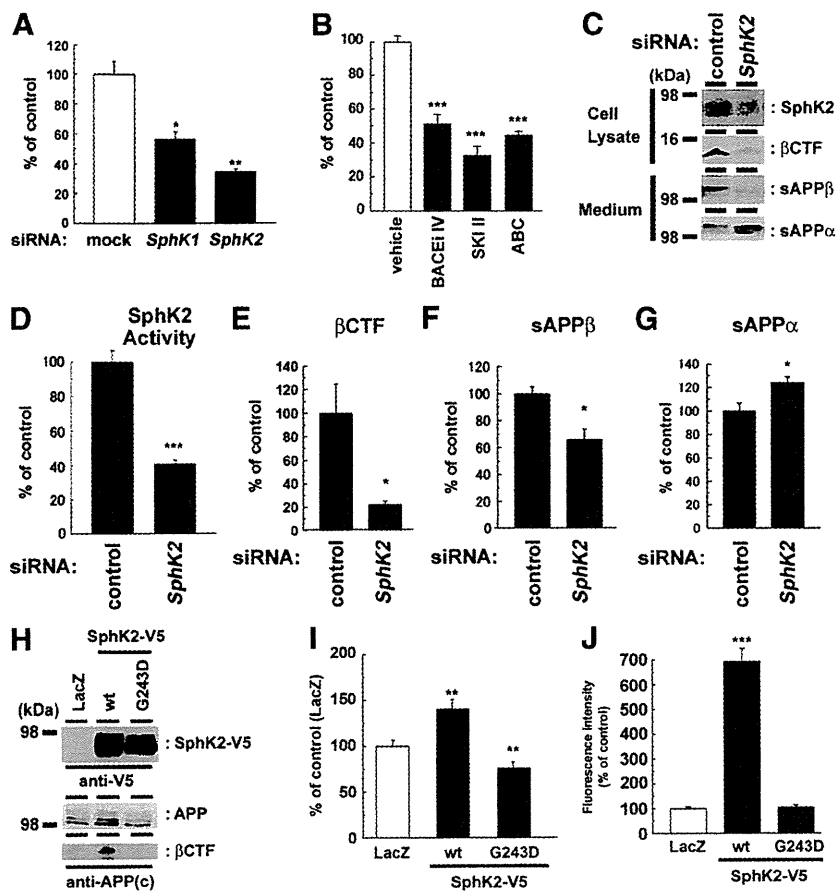
Figure 4. SphK2 activity modulated the β-secretase cleavage products. **A**, N2a cells were transiently transfected with siRNAs against endogenous SphKs. After 48 h transfection, media were replaced and further incubated for 24 h. Levels of secreted Aβ were quantified by ELISA ($n = 3$; mean ± SEM; *$p < 0.05$, **$p < 0.01$). **B**, Levels of secreted Aβ from N2a cells treated with BACE inhibitor IV (BACEi IV), SKI II, or SphK2-selective inhibitor ABC294640 (ABC) for 24 h ($n = 3$; mean ± SEM; ***$p < 0.001$). **C–G**, Effect of transient SphK2 knockdown on APP derivatives in N2a cells. Representative immunoblot analysis was shown in **C**. In vitro SphK2 activity (**D**) as well as βCTF (**E**) in cell lysates and the amount of sAPPβ in conditioned media (**F**) were significantly decreased by knockdown of SphK2. In contrast, the level of sAPPα in conditioned media (**G**) was significantly increased (quantitated by densitometric analysis; $n = 4$; mean ± SEM; *$p < 0.05$). **H–J**, Effect of SphK2 on N2a cells coexpressing Swedish mutant of APP. wt, Wild type. Representative immunoblot analysis was shown in **H**. Overexpression of SphK2, but not inactive mutant (G243D), increased the levels of Aβ production (**I**) as well as SphK2 activity in vitro (**J**) ($n = 4$; mean ± SEM; *$p < 0.05$, **$p < 0.01$).

S1P metabolism coordinately modulates the β-cleavage of APP

To test whether SKI II directly inhibited the enzymatic activity of BACE1, a major β-secretase in neurons, we coincubated SKI II in in vitro assay using recombinant soluble BACE1 corresponding to its extracellular domain. However, SKI II itself did not affect the catalytic activity of recombinant BACE1 (Fig. 3). This result suggests that SKI II modulates the β-cleavage through the inhibition of SphK. Consistently, RNA interference (RNAi) against either SphK1 or 2 significantly decreased the Aβ production in N2a cells (Fig. 4A). Notably, knockdown of SphK2 showed a potent inhibitory effect. Supporting this result, SphK2-selective inhibitor ABC294640 (French et al., 2010) inhibited the Aβ generation in N2a cells similarly to that by SKI II (Fig. 4B), indicating that SphK2 plays a major role in the β-cleavage modulation. Thus, we focused on SphK2 in the following part of the study. RNAi against SphK2 resulted in a significant decrease in the levels of SphK2 expression (Fig. 4C), kinase activity (Fig. 4D), βCTF (Fig. 4E), as well as the secretion of sAPPβ (Fig. 4F), whereas the levels of secreted sAPPα was increased (Fig. 4G). In contrast,

overexpression of SphK2, but not of an inactive mutant (G243D), significantly increased the levels of βCTF and secreted Aβ (Fig. 4H,I), along with an augmentation in SphK2 activity in vitro (Fig. 4J). Notably, coexpression of inactive SphK2 mutant decreased the levels of secreted Aβ (Fig. 4I), indicating that this mutant functions in a dominant-negative manner (Yoshimoto et al., 2003). These data indicate that cellular SphK2 activity is tightly correlated with the β-cleavage of APP.

To further test whether S1P, which is produced by SphK activity, is the regulator of β-cleavage, we examined the effects of S1P degrading enzymes on APP processing. SGPP1 dephosphorylates S1P to sphingosine, and SGPL1 irreversibly cleaves S1P to generate phosphoethanolamine and a long-chain aldehyde (Fig. 5A) (Alvarez et al., 2007; Takabe et al., 2008). Thus, these enzymes decrease the cellular S1P levels with different end products. Overexpression of either SGPP1 or SGPL1 in N2a cells strongly reduced the levels of βCTF and secreted Aβ (Fig. 5B–D). In contrast, the expression of catalytically inactive SGPL1 harboring K353L mutation (Reiss et al., 2004) showed no effect. Moreover, the inhibition of SGPL1 by THI (Schwab et al., 2005) caused a significant increase in Aβ secretion from mouse primary neurons (Fig. 5E), suggesting that the enzymatic activity of S1P degrading enzymes is important for the modulation of β-cleavage. Together, these data indicate that the S1P metabolism coordinately modulates the β-cleavage of APP.

Cell-associated S1P directly modulates BACE1 activity

A proportion of newly synthesized S1P is secreted, whereas others remain associated with cells. In general, extracellular S1P poorly permeates into the cells (Kihara et al., 2003) and functions as a ligand for cell-surface GPCR-type receptors (Alvarez et al., 2007; Takabe et al., 2008). However, extracellular application of S1P failed to restore the reduced Aβ secretion by SKI II treatment or SphK2 knockdown (Fig. 6A,B), suggesting that cell-associated S1P is involved in the regulation of β-cleavage. Next we tested the effect of S1P on the intrinsic activity of membrane-bound BACE1 in a cell-free assay. Both pretreatment of SKI II (Fig. 6C) and SphK2 knockdown (Fig. 6D) on N2a cells significantly decreased the BACE1 activity in the membrane fractions in vitro, implicating that the levels of S1P within cells correlate with BACE1 activity. Supporting this notion, addition of S1P into the microsome fraction significantly increased the intrinsic BACE1 activity (Fig. 6E). These data implicate the direct action of S1P on BACE1 activity rather than the cell-surface receptor-mediated modulation. To provide additional evidence that S1P directly modulates BACE1, we examined binding of endogenous BACE1 in N2a cell lysates to S1P immobilized on agarose beads (Fig. 6F). We confirmed the specific binding of